The Low-redshift Lyman Continuum Survey. I. New, Diverse Local Lyman Continuum Emitters

Sophia R. Flury, Anne E. Jaskot, Harry C. Ferguson, Gábor Worseck, Kirill Makan, John Chisholm, Alberto Saldana-Lopez, Daniel Schaerer, Stephan Mccandliss, Bingjie Wang, et al.

The Astrophysical Journal Supplement Series, 260:1 (17pp), 2022 May https://doi.org/10.3847/1538-4365/ac5331

The Low-redshift Lyman Continuum Survey. I. New, Diverse Local Lyman Continuum Emitters

Sophia R. Flury[1], Anne E. Jaskot[2], Harry C. Ferguson[3], Gábor Worseck[4], Kirill Makan[4], John Chisholm[5], Alberto Saldana-Lopez[6], Daniel Schaerer[6], Stephan McCandliss[7], Bingjie Wang[7], N. M. Ford[2], Timothy Heckman[7], Zhiyuan Ji[1], Mauro Giavalisco[1], Ricardo Amorin[8], Hakim Atek[9], Jeremy Blaizot[10], Sanchayeeta Borthakur[11], Cody Carr[12], Marco Castellano[13], Stefano Cristiani[14], Stephane De Barros[6], Mark Dickinson[15], Steven L. Finkelstein[5], Brian Fleming[16], Fabio Fontanot[14], Thibault Garel[6], Andrea Grazian[17], Matthew Hayes[18], Alaina Henry[3], Valentin Mauerhofer[6], Genoveva Micheva[19], M. S. Oey[20], Goran Ostlin[18], Casey Papovich[21], Laura Pentericci[13], Swara Ravindranath[3], Joakim Rosdahl[10], Michael Rutkowski[22], Paola Santini[13], Claudia Scarlata[12], Harry Teplitz[23], Trinh Thuan[24], Maxime Trebitsch[25], Eros Vanzella[26], Anne Verhamme[6,10], and Xinfeng Xu[7]

[1] Department of Astronomy, University of Massachusetts Amherst, Amherst, MA 01002, USA; sflury@umass.edu
[2] Department of Astronomy, Williams College, Williamstown, MA 01267, USA
[3] Space Telescope Science Institute, 3700 San Martin Drive, Baltimore, MD, 21218, USA
[4] Institut für Physik und Astronomie, Universität Potsdam, Karl-Liebknecht-Str. 24/25, D-14476 Potsdam, Germany
[5] Department of Astronomy, University of Texas at Austin, Austin, TX 78712, USA
[6] Observatoire de Genève, Université de Genève, 51 Ch. des Mailletes, 1290 Versoix, Switzerland
[7] Department of Physics and Astronomy, Johns Hopkins University, Baltimore, MD 21218, USA
[8] Departamento de Física y Astronomía, Universidad de La Serena, Av. Juan Cisternas 1200 Norte, La Serena, Chile
[9] Institut d'astrophysique de Paris, CNRS UMR7095, Sorbonne Université, 98bis Boulevard Arago, F-75014 Paris, France
[10] Univ Lyon, Univ Lyon1, Ens de Lyon, CNRS, Centre de Recherche Astrophysique de Lyon UMR5574, F-69230, Saint-Genis-Laval, France
[11] School of Earth & Space Exploration, Arizona State University, Tempe, AZ 85287, USA
[12] Minnesota Institute for Astrophysics, School of Physics and Astronomy, University of Minnesota, 316 Church Street SE, Minneapolis, MN 55455, USA
[13] INAF, Osservatorio Astronomico di Roma, via Frascati 33, I-00078 Monteporzio Catone, Italy
[14] INAF Osservatorio Astronomico di Trieste, via G.B. Tiepolo 11, I-34143, Trieste, Italy
[15] National Optical-Infrared Astronomy Research Laboratory, Tucson, AZ, USA
[16] Laboratory for Atmospheric and Space Physics, Boulder, CO, USA
[17] INAF-Osservatorio Astronomico di Padova, Vicolo dell'Osservatorio 5, I-35122, Padova, Italy
[18] The Oskar Klein Centre, Department of Astronomy, Stockholm University, AlbaNova, SE-10691 Stockholm, Sweden
[19] Leibniz-Institute for Astrophysics Potsdam, An der Sternwarte 16, D-14482 Potsdam, Germany
[20] Department of Astronomy, University of Michigan, Ann Arbor, MI 48109, USA
[21] George P. and Cynthia Woods Mitchell Institute for Fundamental Physics and Astronomy, Department of Physics and Astronomy, Texas A&M University, College Station, TX, USA
[22] Department of Physics and Astronomy, Minnesota State University, Mankato, MN 56001, USA
[23] Infrared Processing and Analysis Center, California Institute of Technology, Pasadena, CA 91125, USA
[24] Astronomy Department, University of Virginia, Charlottesville, VA 22904, USA
[25] Astronomy, Kapteyn Astronomical Institute, Landleven 12, 9747 AD Groningen, The Netherlands
[26] INAF, Osservatorio Astronomico di Bologna, via Gobetti 93/3, I-40129 Bologna, Italy
Received 2021 August 5; revised 2021 December 14; accepted 2022 January 7; published 2022 April 21

Abstract

The origins of Lyman continuum (LyC) photons responsible for the reionization of the universe are as of yet unknown and highly contested. Detecting LyC photons from the Epoch of Reionization is not possible due to absorption by the intergalactic medium, which has prompted the development of several indirect diagnostics to infer the rate at which galaxies contribute LyC photons to reionize the universe by studying lower-redshift analogs. We present the Low-redshift Lyman Continuum Survey (LzLCS) comprising measurements made with the Hubble Space Telescope Cosmic Origins Spectrograph for a $z = 0.2$–0.4 sample of 66 galaxies. After careful processing of the far-UV spectra, we obtain a total of 35 Lyman continuum emitters (LCEs) detected with 97.725% confidence, nearly tripling the number of known local LCEs. We estimate escape fractions from the detected LyC flux and upper limits on the undetected LyC flux, finding a range of LyC escape fractions up to 50%. Of the 35 LzLCS LCEs, 12 have LyC escape fractions greater than 5%, more than doubling the number of known local LCEs with cosmologically relevant LyC escape.

Unified Astronomy Thesaurus concepts: Reionization (1383); Galactic and extragalactic astronomy (563); Ultraviolet astronomy (1736); Hubble Space Telescope (761)

Supporting material: figure sets, machine-readable tables

1. Introduction

Numerous observations in the last decade indicate that the universe was reionized by a redshift of $z \approx 6$. The Gunn–Peterson effect observed as an absorption trough in the continua of distant quasars (e.g., Gunn & Peterson 1965; Becker et al. 2001) and as the absorption of Lyα photons (e.g., Fan et al. 2006; Yang et al. 2020), the optical depth of the cosmic microwave background in

the form of Thomson scattering (e.g., Paoletti et al. 2020; Planck Collaboration et al. 2020), and the reduced transmission of Lyα observed at higher redshifts (e.g., Mason et al. 2018; Pahl et al. 2020) all demonstrate that the intergalactic medium (IGM) transitions from neutral to ionized near this redshift.

While the state of reionization is clear, the nature of the objects that regulated and dominated this process is not. Dwarf galaxies ($M_\star \lesssim 10^9 M_\odot$), which have weaker gravitational potentials, are more susceptible to clearing of attenuating material by stellar winds and supernovae (SNe), thereby increasing the fraction of Lyman continuum (LyC) photons that escape their host galaxy (e.g., Razoumov & Sommer-Larsen 2010; Wise et al. 2014; Paardekooper et al. 2015). However, more massive galaxies have the gas reservoirs necessary for high star formation rate (SFR) densities and experience less suppressive feedback from stellar winds and supernovae, allowing more stars to form and, ergo, more LyC photon production (Wyithe & Loeb 2013).

Which galaxy mass regime dominates reionization is a matter of some contention. Current empirically motivated models suggest relatively more luminous (albeit still faint) galaxies are the primary, if not sole, source of escaping LyC photons responsible for reionization (Naidu et al. 2020). Other models predict less luminous galaxies dominate reionization (e.g., Finkelstein et al. 2019), owing largely to steeper luminosity functions than those adopted by Naidu et al. (2020). Local observations of LyC (e.g., Izotov et al. 2018b) seem to favor the dwarf-galaxy scenario suggested by radiation hydrodynamical simulations (e.g., Trebitsch et al. 2017) as do some holistic models incorporating massive galaxies, active galactic nuclei (AGNs), and dwarf galaxies (e.g., Finkelstein et al. 2019; Dayal et al. 2020).

Although star-forming galaxies remain the most likely candidates for reionization, their exact contribution is still unknown. One of the least constrained parameters in our understanding of reionization is the so-called escape fraction $f_{\rm esc}^{\rm LyC}$, the fraction of LyC photons that escape from the host galaxy into the IGM (Steidel et al. 2001). As it pertains to reionization, $f_{\rm esc}^{\rm LyC}$ relates to the cosmic ionization rate by

$$\dot{n}_{\rm gal} = f_{\rm esc}^{\rm LyC}\,\xi_{\rm ion}\,\rho_{\rm SFR} \quad (1)$$

where $\dot{n}_{\rm gal}$ is the emission rate of LyC photons by high-redshift ($z \geqslant 6$) galaxies per unit comoving volume, $\xi_{\rm ion}$ is the total rate of LyC photons produced within their progenitor galaxies per SFR, and $\rho_{\rm SFR}$ is the volume density of galaxies per unit SFR. All properties on the right-hand side of Equation (1) may vary with other galaxy properties such as galaxy mass. Further complicating constraints on $\dot{n}_{\rm gal}$ is the fact that, whereas $\rho_{\rm SFR}$ can be inferred from observations, $f_{\rm esc}^{\rm LyC}$ is degenerate with $\xi_{\rm ion}$ if measured from Balmer emission lines, which complicates estimating $f_{\rm esc}^{\rm LyC}$ from LyC measurements. Some constraint on $\xi_{\rm ion}$, such as Hα or [O III]λ5007 (e.g., Bouwens et al. 2016; Schaerer et al. 2016), is necessary to break this degeneracy (e.g., Steidel et al. 2018). Values of $f_{\rm esc}^{\rm LyC}$ required by reionization models typically span 0.1 (Finkelstein et al. 2015, 2019) to 0.2 (Robertson et al. 2015; Naidu et al. 2020).

Unfortunately, observational constraints on $f_{\rm esc}^{\rm LyC}$ have proven difficult to obtain. Early space-based LyC observations of local galaxies yielded upper limits (Leitherer et al. 1995; Deharveng et al. 2001), suggesting $f_{\rm esc}^{\rm LyC} \lesssim 3\%$. Many putative detections at higher redshifts ($z \sim 3$) over the next 10 yr turned out to be non-LyC contamination from lower-redshift interlopers at small angular separation (e.g., Vanzella et al. 2012; Mostardi et al. 2015; Siana et al. 2015). Another difficulty stems from IGM attenuation at higher redshifts, which (i) makes LyC measurements at or beyond reionization ($z \gtrsim 6$) impossible because all of the LyC photons are absorbed (e.g., Becker et al. 2021); and (ii) makes imaging detections of the LyC at moderately high redshifts ($z = 2$–3) complicated because the Lyman series and LyC attenuation are uncertain along any particular line of sight (e.g., Inoue et al. 2014; Steidel et al. 2018). Moreover, the LyC is too faint at $z \gtrsim 4$ to be detected with even the largest contemporary ground-based telescopes.

Despite these complications, the past several years have enjoyed an explosion of LyC detections from a few upper limits to a few tens of significant measurements. Observations of local ($z < 0.4$) galaxies with the Hubble Space Telescope (HST) Cosmic Origins Spectrograph (COS; Green et al. 2012) have yielded $\gtrsim$16 LyC detections (Leitet et al. 2013; Borthakur et al. 2014; Leitherer et al. 2016; Izotov et al. 2016a, 2016b, 2018a, 2018b; Wang et al. 2019; Izotov et al. 2021). These measurements are not without difficulty: scattered telluric light can contaminate the LyC (see Chisholm et al. 2017 regarding Leitherer et al. 2016) and even masquerade as LyC (see Izotov et al. 2016b, regarding FUSE observations by Leitet et al. 2013).

Of the best measurements of the LyC from local galaxies, the Green Peas (GPs), which in many ways resemble galaxies in early cosmological epochs (e.g., Cardamone et al. 2009; Amorín et al. 2010, 2012; Jaskot & Oey 2013; Schaerer et al. 2016), exhibit $f_{\rm esc}^{\rm LyC}$ that can exceed 20% (e.g., Izotov et al. 2018b). Ground-based observations have made significant headway at higher redshifts ($z \sim 3$) with careful measurements of $f_{\rm esc}^{\rm LyC}$ for 16 galaxies (Steidel et al. 2018; Vanzella et al. 2018). Further HST observations have contributed to the $z \sim 3$ measurements of $f_{\rm esc}^{\rm LyC}$ by adding $\gtrsim$10 LyC detections (Mostardi et al. 2015; de Barros et al. 2016; Vanzella et al. 2016; Bian et al. 2017; Micheva et al. 2017; Fletcher et al. 2019; Rivera-Thorsen et al. 2019; Ji et al. 2020).

The search for Lyman continuum emitters (LCEs; sometimes referred to as Lyman continuum "leakers," e.g., Bergvall et al. 2013) at high redshift relies on indirect indicators of the physical mechanisms involved in LyC escape. The [O III]λ5007/[O II]$\lambda\lambda$ 3726,29 (O_{32}) emission line flux ratio, thought to be a proxy for optical depth in extreme GP galaxies (e.g., Jaskot & Oey 2013; Nakajima & Ouchi 2014), has successfully been used to select LCE candidates for two HST/COS observing programs (Izotov et al. 2016a, 2016b, 2018a, 2018b). However, a third observing program using O_{32} as a selection criterion, Izotov et al. (2021), did not reproduce this success. SFR surface density ($\Sigma_{\rm SFR}$) can gauge the role of stellar feedback in facilitating LyC escape (e.g., Heckman et al. 2001; Clarke & Oey 2002). Indeed, cosmological simulations predict that $\Sigma_{\rm SFR}$ correlates with $f_{\rm esc}^{\rm LyC}$ where $\Sigma_{\rm SFR} > 0.1\ M_\odot\ {\rm yr}^{-1}\ {\rm kpc}^{-2}$ corresponds to cosmologically relevant values of $f_{\rm esc}^{\rm LyC} \gtrsim 5\%$ (e.g., Sharma et al. 2017; Naidu et al. 2020). Extinction and starburst age determine the slope (measured by the spectral index assuming $f_\lambda \propto \lambda^\beta$) of the nonionizing UV continuum. Values of $\beta \lesssim -2$ indicate young (<30 Myr), unextinguished stellar populations from which LyC photons could escape (e.g., Zackrisson et al. 2013, 2017). Together, O_{32}, $\Sigma_{\rm SFR}$, and β can serve as holistic selection criteria for LCE candidates, although these properties may select galaxies with intrinsically strong LyC flux rather than galaxies with high $f_{\rm esc}^{\rm LyC}$.

This paper presents the Low-Redshift Lyman Continuum Survey (LzLCS). We have assembled a sample of 66 star-forming galaxies from the Sloan Digital Sky Survey (SDSS; York et al. 2000) and the Galaxy Evolution Explorer (GALEX; Martin et al. 2003) that reside nearby ($z \sim 0.3$) and are considered likely candidates for LyC escape according to the above criteria (Section 2). We have observed each of these 66 galaxies with HST/COS to measure the LyC (Sections 3–4). From the HST/COS and SDSS photometry and spectra, we derive physical and observational properties to characterize these 66 galaxies and compare them to a set of LCEs from the literature that have been previously observed with HST/COS (Section 5). From our measurements of the LyC flux, we provide estimates of $f_{\rm esc}^{\rm LyC}$ for our sample (Section 6). Companion papers present our initial tests of indirect LyC diagnostics (Flury et al. 2022; Saldana-Lopez et al. 2022; Wang et al. 2021). Throughout this paper, we assume $H_0 = 70$ km s^{-1} Mpc^{-1}, $\Omega_m = 0.3$, and $\Omega_\Lambda = 0.7$.

2. Sample Definition

We define a sample of 66 LCE candidates, the LzLCS, to investigate the properties, physical mechanisms, and diagnostics associated with LyC escape. To begin, we search for star-forming galaxies in the SDSS Data Release 15 (Blanton et al. 2017) using either the tabulated emission line fluxes or our own measurements made following Jaskot et al. (2019). We limit our sample to star-forming galaxies by using the [O III]/Hβ vs. [N II]/Hα emission line diagnostic (the Baldwin–Phillips–Terlevich diagram; Baldwin et al. 1981) to exclude AGN and composite systems. Then, we match these objects with photometry from the GALEX data archive. We select galaxies that are relatively nearby ($z \sim 0.3$) so that the rest-frame LyC can be readily observed by HST/COS with the G140L grating while reaching the sensitivity required to detect $f_{\rm esc}^{\rm LyC} \sim 5\%$ at signal-to-noise ratio (S/N) > 5 for each object. The COS throughput imposes a redshift limit of $z \gtrsim 0.22$ to this detection goal because its sensitivity declines by roughly two orders of magnitude for wavelengths below 1100 Å (Green et al. 2012).

From the SDSS-GALEX star-forming galaxies, we select objects to evenly sample the O_{32}, β, and $\Sigma_{\rm SFR}$ methods of inferring $f_{\rm esc}^{\rm LyC}$ with ∼50 objects each across a range of the relevant parameter space. The LzLCS is thus designed to span a far wider range of relevant parameter spaces than previous investigations, allowing us to determine whether LCEs are a heterogeneous or homogeneous population of galaxies.

We include 37 objects from the low-redshift SDSS/GALEX with $O_{32} > 3$, bringing the number of objects with high O_{32} to 50 when combined with previous studies. We include an additional 29 galaxies with high SFR surface densities (lower limit of $\Sigma_{\rm SFR} > 0.1$ $M_\odot$ yr^{-1} kpc^{-2} estimated from the dust-corrected GALEX FUV magnitude assuming $A_{FUV} \sim 12 \times E(B-V)$ and SDSS u-band half-light radius) and/or blue UV continua (power-law index $\beta < -2$ estimated from the GALEX photometry). We chose galaxies with various combinations of these criteria to improve the chances of targeting true LCEs. As a result, at least 37 galaxies in the total sample satisfy each criterion, with 11 galaxies satisfying all three (Figure 1).

3. Observations with HST/COS

For the sample of 66 candidate LyC-leaking galaxies, we obtained 134 orbits of HST/COS spectroscopy under observing program GO 15626 (Cycle 26, P.I. Jaskot). COS acquires each object via near-UV (NUV) imaging and centered its 2.″5 diameter spectroscopic aperture on the peak NUV flux. We used the G140L grating at 800 Å in COS Lifetime Position 4, covering a wavelength range of 800–1950 Å with a resolution of $R \sim 1050$ at 1100 Å (see Izotov et al. 2021). We show a log of the observations in Table 1 and example acquisition images in Figure 2.

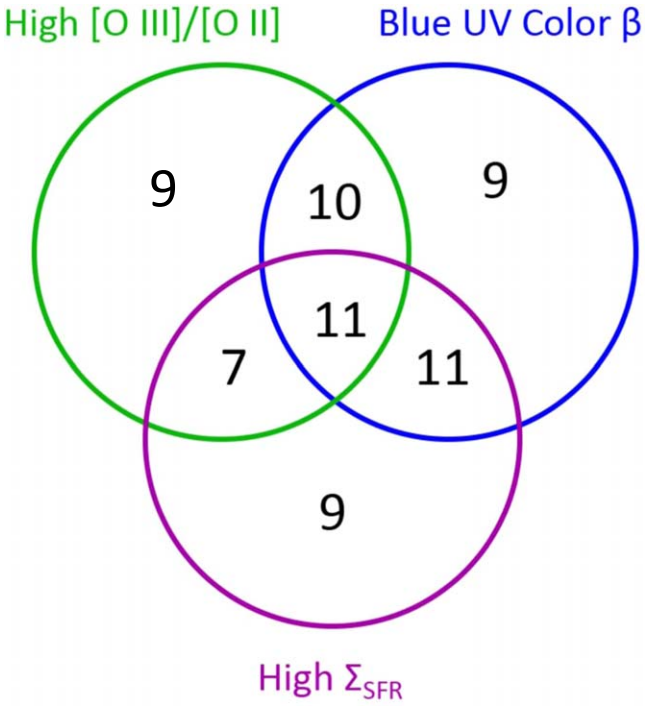

Figure 1. Venn diagram showing the overlap of the three selection criteria for the LzLCS: O_{32} = [O III]/[O II] flux ratio (top left), UV slope parameterized by spectral index β (top right), and star formation rate surface density $\Sigma_{\rm SFR}$ (bottom center).

Following previous works (Worseck et al. 2016; Izotov et al. 2018b; Wang et al. 2019; Izotov et al. 2021), we process the raw HST/COS spectra using a combination of standard and custom software to best model the background and optimize measurement of the LyC. The COS detector measures the pulse height amplitude (PHA) of charge produced by an amplifying microchannel plate. Dark current and location-dependent geomagnetic activity like the South Atlantic Anomaly can trigger the COS detector, resulting in spurious background events with a PHA distribution extending beyond PHAs of science events (Worseck et al. 2016; Izotov et al. 2016b). Before processing the spectra, we screen PHAs to include only values within the 1–12 range for Lifetime Position 4 to mitigate dark current and other background effects without excluding science events. We reduce the spectra using the CALCOS pipeline (v3.3.9) to perform flat-fielding, dead time and stim pulse corrections, and wavelength and flux calibrations. For the extraction, we draw a rectangular aperture 25 pixels wide along the cross-dispersion axis (hatched region in Figure 4), a range comparable to the 95th percentiles of the total starlight continuum profile after excluding geocoronal Lyα emission.

With the custom software FAINTCOS (Worseck et al. 2016; Makan et al. 2021)[27], we estimate the dark current and scattered geocoronal Lyα background and coadd individual exposures to

[27] https://github.com/kimakan/FaintCOS

Table 1
HST/COS Observation Log for the LzLCS

Object	R.A. (deg)	Decl. (deg)	z	Visit	Date	Exp. Time (s)	No. Darks
J003601+003307	9.002641	0.552006	0.3479	ldxe08	2019-09-25	3980.384	13
J003601+003307	9.002641	0.552006	0.3479	ldxew9	2019-12-08	3980.672	9
J004743+015440	11.928487	1.911086	0.3535	ldxe42	2019-07-29	1495.904	9
J011309+000223	18.286905	0.039839	0.3062	ldxez5	2019-08-03	1363.904	13
J012217+052044	20.569425	5.345561	0.3656	ldxe05	2019-09-20	3780.320	15

Note. Also indicated are the average number of dark current observations used to model the background dark current in each visit.
(This table is available in its entirety in machine-readable form.)

improve S/Ns while preserving Poisson counts. For each observation, we compare the PHA cumulative distribution function of each dark current observation obtained from a ± 1 month window, selecting those that match the PHA cumulative distribution function of the background in the science image by means of a Kolmogorov–Smirnoff test ($D < 0.03$) to ensure the solar and geomagnetic conditions during the recording of the dark current are comparable to those of the science image (Worseck et al. 2016; Izotov et al. 2018b). We show the number of dark observations selected in this manner for each visit in Table 1. To evaluate the success of the dark model, we compare the spatial variations of the dark model to the background of the science image and find that the two consistently agree (see gray line in Figure 4). We scale the Worseck et al. (2016) model for scattered light background by the peak telluric Lyα counts in each extraction. We co-add the spectra and background models for each object and bin from the oversampled detector dispersion of 0.0803–0.5621 Å in order to Nyquist-sample the G140L resolution of ~1.1 Å. In cases where the gross counts are less than 100 counts above the background, we determine the Neyman–Pearson 1σ confidence intervals in the flux measurements following Feldman & Cousins (1998). Otherwise, we sample variates from the Poisson distributions of the background and science spectra to compute the 1σ confidence in the flux in each pixel. Finally, we correct each spectrum for Milky Way extinction using Galactic $E(B-V)$ estimates from the dust maps by Green et al. (2018) and the Fitzpatrick (1999) extinction law. To determine the final uncertainty in the corrected flux in each pixel, we sample flux measurements and the Green et al. (2018) reddening 10^4 times.

4. Measuring Lyman Continuum

We measure the LyC flux in a rest-frame 20 Å window as close as possible to $\lambda_{\rm rest} = 900$ Å while avoiding wavelengths above $\lambda_{\rm obs} = 1180$ Å to minimize telluric contamination, rounding down to the nearest 10 Å in the rest frame. This constraint ensures as uniform a measurement of the LyC as possible across the entire sample while simultaneously preventing any contamination by the Lyα and N I λ1200 geocoronal emission lines or by non-LyC starlight introduced into the 900–912 Å range by dispersion through the HST/COS optics. To evaluate any unresolved geocoronal contamination, we compare the count rate during orbital night to that of the total visit and find good agreement between the two, indicating no significant contributions of telluric radiation to the LyC. Moreover, the scattered light model by Worseck et al. (2016) rectifies minor discrepancies between the two count rates, indicating that our treatment of the background light is appropriate.

Table 2
LzLCS and Published Detections of Local LCEs with HST/COS

Quality	Signif.	Max. $P(>N\|B)$	LzLCS	Pub.
Good	>5	2.867×10^{-7}	12	14
Fair	3–5	1.350×10^{-3}	13	0
Marginal	2–3	2.275×10^{-2}	10	1
Detected	>2	2.275×10^{-2}	35	15
Upper limit	⩽2	1	31	8

Note. Significance is the number of Poisson standard deviations between the measured LyC counts and the model background counts. $P(>N|B)$ is the probability of measuring LyC counts greater than those measured in the COS spectrum given the background counts. LzLCS indicates the number of galaxies from the LzLCS corresponding to each detection criterion. "Pub." indicates the number of galaxies from HST/COS observations published in the literature and reprocessed by the LzLCS collaboration.

We consider the mean background-subtracted flux density in the spectral window to be the LyC flux, $F^{\rm obs}_{\lambda \rm LyC}$, and the 84th percentile in the background distribution (i.e., the 1σ sensitivity limit) to be the upper limit on $F^{\rm obs}_{\lambda \rm LyC}$ in cases of nondetections. As a robust assessment of detection, we determine the probability, $P(>N|B)$, that the total observed, or gross, counts N within the spectral window are realized from the distribution of background counts B. Worseck et al. (2016) defined $P(>N|B)$ as the survival function for the Poisson distribution of the background counts evaluated at the gross observed counts. Proceeding with this convention, the probability that the gross measured LyC counts N are a chance realization of the background B is

$$P(>N|B) = 1 - \mathrm{Q}(N+1, B) \quad (2)$$

where Q is the regularized incomplete gamma function. We consider $P(>N|B) = 0.02275$, the 2σ value given by the normal distribution survival function, an acceptable maximum probability that the observed counts are sampled from the background. We list the number of galaxies in the LzLCS that satisfy traditional 2σ, 3σ, and 5σ detection criteria in Table 2 and provide examples of the rest-frame LyC for non-, weak (~2σ), and strong ($\gtrsim 5\sigma$) detections in Figure 3. In total, 35 galaxies satisfy our detection requirements.

To confirm these detections, we examine the cross-dispersion profile of the two-dimensional spectrum in the LyC window to qualitatively verify the presence of an LyC profile that appears roughly consistent with the non-LyC starlight profile. We show such a comparison of LyC with the non-LyC starlight profile in Figure 4. In summary, we detect 35 LCEs

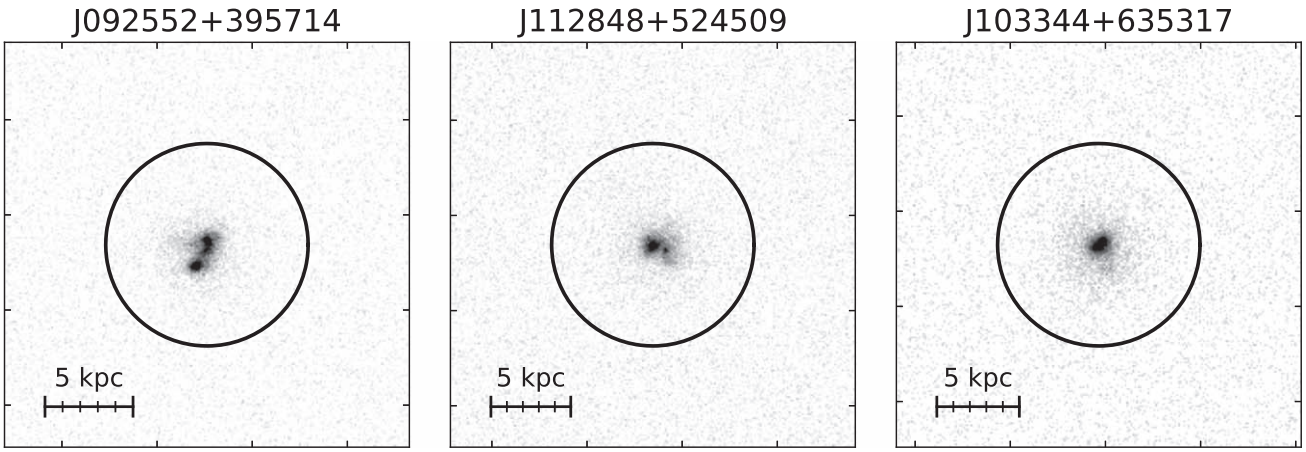

Figure 2. Example log-scaled acquisition images of a nonemitter (left), marginally detected LCE (center) and well-detected LCE (right) from the LzLCS. The circle indicates the 2.″5 COS spectroscopic aperture. The bar in the bottom left indicates a physical scale of 5 kpc at the target's redshift with 1 kpc ticks.

(The complete figure set (66 images) is available.)

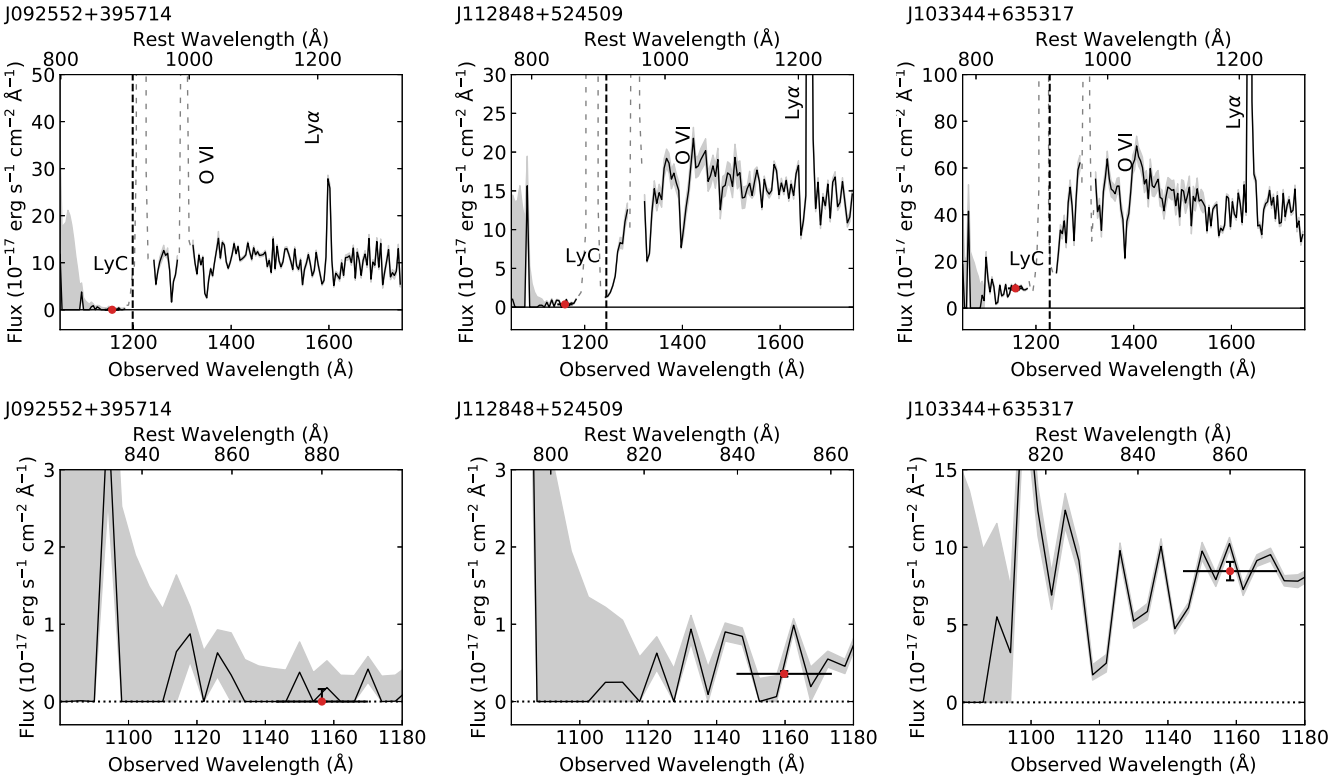

Figure 3. Top: example spectra (black) of a nonemitter (left), marginally detected LCE (center) and well-detected LCE (right) from the LzLCS, downsampled to 4 Å resolution for visualization. The gray shaded region indicates the 1σ uncertainty in flux density. The red circle is the measured LyC flux with black lines showing the 68% confidence intervals (capped) and rest-frame 20 Å spectral bin (uncapped). Gray broken lines indicate the clipped geocoronal emission from telluric Lyα and O I. The dashed vertical line indicates the Lyman limit. Bottom: the same as top but with the LyC region magnified.

(The complete figure set (66 images) is available.)

out of 66 targets. We show the LzLCS LyC fluxes in Figure 5 as a function of redshift to highlight the effect of changes in COS sensitivity across the detector.[28]

To ensure consistency in our method, we reprocess the raw HST/COS spectra for the 23 galaxies in the Izotov et al. (2016a, 2016b, 2018a, 2018b, 2021) and Wang et al. (2019) investigations of local ($z \lesssim 0.4$) LCE candidates following the same procedure and find that we reproduce their LyC fluxes. The median relative difference between the published fluxes and our measurements is $0.094^{+0.043}_{-0.022}$, indicating that we recover their results to within 10% but with a statistically significant difference. While the scatter and differences are small, this

[28] We estimate that pending changes to the COS flux calibration, which are not yet public for our Lifetime Position 4 settings, will result in a 6%–6.5% increase in our measured LyC flux and a smaller increase in flux at longer wavelengths. However, this increase is comparable to the relative uncertainty in the measured flux and will only increase the corresponding $f_{\rm esc}^{\rm LyC}$ by a factor of ∼1.02.

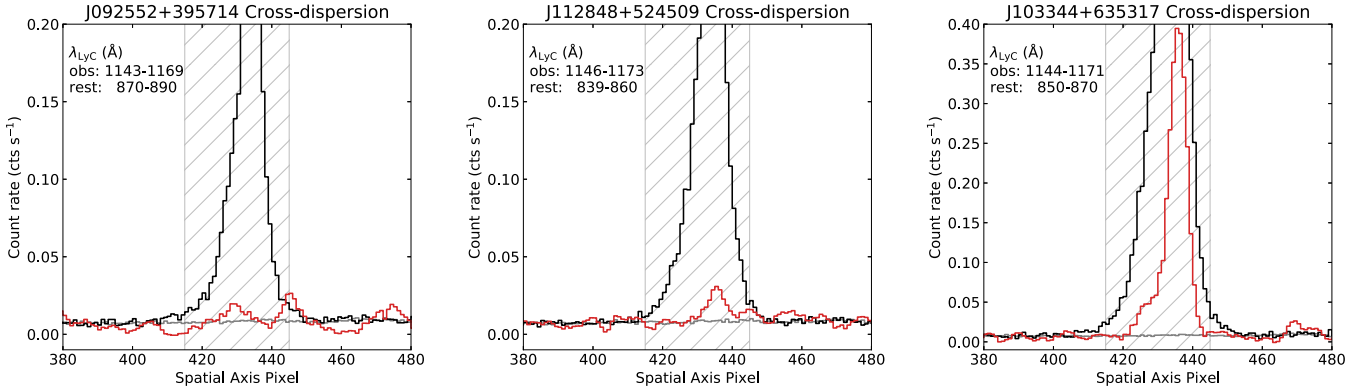

Figure 4. Example spatial cross section of the two-dimensional spectrum for a nonemitter (left), marginally detected LCE (center) and well-detected LCE (right) from the LzLCS. The black line represents the nonionizing starlight continuum, the gray line represents the model dark current, red line represents the LyC scaled to the same median background counts as the starlight profile, and the gray hatched stripe represents the spectral extraction aperture.

slight disagreement suggests our reprocessing and re-measurement of the Izotov et al. (2016a, 2016b, 2018a, 2018b, 2021) and Wang et al. (2019) LyC fluxes are necessary to mitigate any systematic discrepancies. Because we used the same custom reduction software, we attribute the difference to a combination of the spectral window over which we measure the LyC. We find 15 of the 23 Izotov et al. (2016a, 2016b, 2018a, 2018b, 2021) and Wang et al. (2019) LCE candidates satisfy our detection requirements. For the 23 LCE candidates, our significance assessment is consistent with the literature; however, we consider two objects, J124810+425954 (Izotov et al. 2018b) and J112721+461042 (Izotov et al. 2021), to be nondetections because our detection requirement is more stringent. Both we and the authors report 1σ LyC detection significance in these instances. We present the LyC fluxes for these published LCE candidates with the LzLCS results in Figure 5.

Thus, the 35 detections in the LzLCS sample nearly triple the total number of confirmed LCEs in the local universe.

5. LzLCS Galaxy Properties

Below, we detail the measurement and calculation of various properties of the LzLCS galaxies and compare them to the same properties for the 23 local ($z \lesssim 0.4$) galaxies discussed in Section 4 with HST/COS observations of the LyC published in Izotov et al. (2016a, 2016b, 2018a, 2018b, 2021) and Wang et al. (2019). Furthermore, we demonstrate the much broader range of the LzLCS properties relative to previous LCE surveys. We list these properties in Tables 3–8 for several LzLCS targets and provide the full machine-readable tables of these properties online.

5.1. Optical Extinction

We have measured fluxes and equivalent widths (EWs) of emission lines in the SDSS DR15 spectra by fitting them with one to two Gaussian profiles following Jaskot et al. (2019). In some cases, the [O III]λ5007 profile appears "sheared off" or affected by sky lines, and the [O III] F_{5007}/F_{4959} flux ratio deviates significantly from the expected ratio of 2.98 (Storey & Zeippen 2000). In these cases, we adopt $F_{5007} = 2.98F_{4959}$. We convert the observed EWs to the rest frame using redshifts obtained from the SDSS. Using the dust maps by Green et al. (2018) and the Fitzpatrick (1999) extinction law, we correct the observed-frame emission line fluxes for Galactic extinction. Then, we iteratively compute the uncertainty-weighted rest-frame internal $E(B-V)$ and stellar absorption from the Hα, Hβ, Hγ, Hδ, and Hε emission line fluxes and EWs if the emission line flux is detected at S/N > 5. Correction for stellar absorption is adapted from Equation (1) from Izotov et al. (1994). In the seven cases where the Hα/Hβ is more than one standard deviation below the Case B value of 2.747 (Storey & Hummer 1995; assuming the extreme case of $T_e = 2 \times 10^4$ K and $n_e = 10^2$ cm^{-3}) and the four cases where the Hα profile appears sheared off (likely due to spurious cosmic-ray clipping or saturation), we exclude Hα from the procedure.

We iterate the following procedure until converging on a solution for $E(B-V)$: (i) derive the electron temperature and density from nebular lines, (ii) calculate the intrinsic flux ratios from the results of step (i) by interpolating over the grid of recombination coefficients from Storey & Hummer (1995), and (iii) compute the variance-weighted average $E(B-V)$ from the ratio of observed to intrinsic Balmer decrements. Electron temperature and density derivation follows the temperature-scaling approach described by Flury & Moran (2020) with collisional populations and emissivities computed by PYNEB (Luridiana et al. 2015). For the electron temperature, we use the [O III] $\lambda\lambda$4363; 4959,5007 auroral line and nebular doublet, substituting the [O III] λ4363 flux inferred from the "ff–relation" by Pilyugin et al. (2006) for the 12 galaxies in the total LzLCS sample where the auroral line is not detected (see discussion in Curti et al. 2017). For the electron density, we use the [S II] $\lambda\lambda$6716, 31 doublet, available for 56 galaxies, as the [O II] $\lambda\lambda$3726, 29 doublet is not resolved in the SDSS spectra. Otherwise, we assume $n_e = 100$ cm^{-3}. We assume the Cardelli et al. (1989) extinction law as this choice gives $E(B-V)$ values comparable to other extinction laws (e.g., Gordon et al. 2003) and appropriately describes the extinction of nebular emission lines in LCEs such as the GPs (Izotov et al. 2017).

These corrected flux measurements from the optical spectra provide the Hβ EW (accounting for stellar absorption) and O_{32} flux ratios (accounting for extinction). We show the Hβ EW for the LzLCS galaxies and published LCEs in Figure 6. Values range from 11 to 426 Å with a median of 91 Å. For the LzLCS galaxies and published LCEs, $\log_{10}O_{32}$ spans −0.32 to 1.56 with a median of 0.65, as we show in Figure 7. From both figures, the previously published LCE Hβ EWs and O_{32} ratios are located toward the high end of the LzLCS sample distribution. In other words, the LzLCS extends to much lower Hβ EWs and O_{32} than these previous studies. The LzLCS

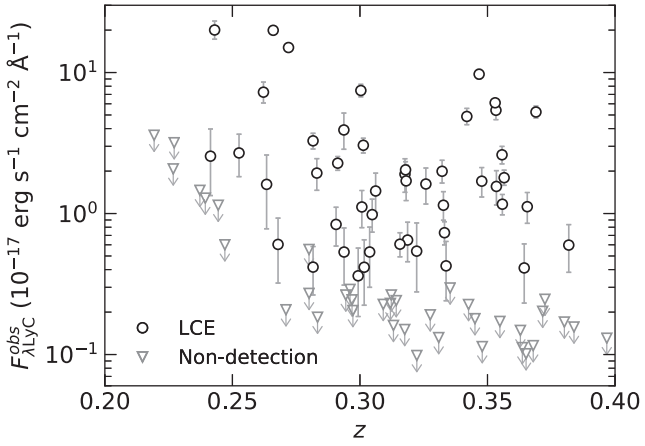

Figure 5. LyC measurements (circles) and upper limits (triangles) for the combined LzLCS and published samples show the HST/COS LyC flux sensitivity limits as a function of redshift. The increase in sensitivity with redshift is due primarily to the location of the LyC on the COS detector.

nearly doubles the number of detected low-redshift LCEs with Hβ EWs > 100 Å and $O_{32} > 3$. Moreover, the LzLCS dramatically improves the number of detected low-redshift LCEs with Hβ EWs < 100 Å and $O_{32} < 3$, a space previously sampled by just three LCEs. The presence of LCEs across such a wide range of EW Hβ suggests galaxies with a variety of burst ages and/or star formation histories can leak LyC photons. Similarly, the presence of LCEs across nearly 2 dex in O_{32} indicates that LCEs span a wide range of ionization parameters and/or nebula boundary conditions.

5.2. Nebular Abundances

With the electron temperatures and densities derived above, we determine direct-method relative oxygen abundances from emissivities computed by PYNEB and extinction-corrected optical emission lines. Monte Carlo sampling the emissivities using the uncertainties in the fluxes, temperatures, and densities yields the total statistical uncertainty in our direct-method abundances. As is evident in Figure 8, the LzLCS spans a range of about 6% to 60% solar oxygen abundance (as defined by Steffen et al. 2015) while the published LCEs are more narrowly concentrated to a range of 10% to 30% solar. The LzLCS samples higher metallicities than previous studies, with ∼50% of the galaxies having $12 + \log_{10}(O/H)$ above the highest published local LCEs. Furthermore, the LzLCS increases the number of detected low-redshift LCEs across all abundances, particularly above $12 + \log_{10}(O/H) \sim 8.2$, demonstrating that, as with Hβ EWs, LCEs span a wide range of star formation histories because $12 + \log_{10}(O/H)$ traces the net number of type II SNe.

5.3. Half-light Radius

Using the reduced MIRROR-A NUV COS acquisition images, we compute the source radius r_{50} containing 50% of the background-subtracted counts. We estimate the median background counts in an annulus centered on the source with an inner radius of 53 pixels to avoid contamination by the source and subtract the median counts from the image. After background subtraction, we correct for vignetting effects. While the galaxies in the LzLCS are typically compact (typical uncorrected galactic profile FWHM $\lesssim 0\farcs4$ in the NUV), we correct the acquisition images for the radial decline in throughput because the total source counts can still be affected by vignetting. Then, we compute the total source counts by measuring the counts enclosed by a range of radii until the total counts vary by less than the rms of the background noise. We then interpolate over the count distribution to obtain the radius at half the total source counts. Uncertainty in the half-light radius is determined by summing the Poisson error of the gross counts, the COS acquisition image plate scale of $0\farcs0235$ px^{-1}, and a maximum NUV imaging PSF FWHM of 2.4 px.

In Figure 9, we show that the UV-emitting stellar populations inhabit small regions with $0.3 < r_{50} < 0.6$ kpc in both the published LCEs and half of the LzLCS galaxies. While the number of galaxies in each bin decreases quickly with increasing half-light radius, the LzLCS galaxies have r_{50} as high as 2.25 kpc, indicating the survey includes galaxies with spatially extended star formation. However, as in previous studies, the LzLCS finds that LCEs predominantly have compact star-forming regions. To confirm this result, we also fit the surface brightness distributions with two-dimensional Sérsic and exponential profiles and find close agreement between the best-fit effective radii and the model-independent half-light radii.

5.4. Lyα and Continuum Properties

The HST/COS spectra are extracted and reduced a second time following the procedure discussed in Section 3, this time using a 30 pixel aperture ($0\farcs637$) in place of the 25 pixel aperture to include more signal because Lyα is more spatially extended than the UV continuum (e.g., Guaita et al. 2015; Wisotzki et al. 2016; Leclercq et al. 2017; Rasekh et al. 2021) and requires less background exclusion than the LyC. For the LzLCS, the Lyα extraction aperture radius corresponds to a factor of about 2.6 more than the UV continuum half-light radius and thus should contain most of the Lyα flux (e.g., Hayes et al. 2013), although vignetting of the COS aperture may exclude some of the Lyα even in the more compact sources. We process the data using the same assumptions as in the previous section, most notably the same Galactic extinction. From these wider extractions, we measure the integrated galactic Lyα flux. We fit the continuum within 100 Å of Lyα with a linear fit using iterative sigma clipping to exclude noise spikes and absorption features, conservatively assuming a 25% uncertainty in the continuum fit. We then integrate the continuum-subtracted flux density where the Lyα feature deviates from the continuum to obtain the Lyα flux, masking the 1206 Å and 1240 Å features to avoid contamination. To obtain the rest-frame Lyα EW, we divide by the continuum flux and correct for redshift. We do not correct for stellar Lyα absorption as its effect on the measured emission line flux and EW is, at most, relatively small (Peña-Guerrero & Leitherer 2013).

In Figure 10, we show the Lyα EWs for the LzLCS and Izotov et al. (2016a, 2016b, 2018a, 2018b, 2021) and Wang et al. (2019) LCE candidates. The LzLCS Lyα EWs $\gtrsim 60$ Å are consistent with the majority of published LCEs; however, 45 of the 66 galaxies in the LzLCS sample have EWs smaller than this value. As with Hβ, we find that LCEs span a wider range in Lyα EWs than previous studies. Because Lyα is more sensitive to the H I column density and the corresponding continuum is more sensitive to recent star formation, the LzLCS results demonstrate that LCEs span a wider range of burst ages and/or

Table 3
Flux Ratios Measured from the SDSS Optical Spectra for the Combined LzLCS and Izotov et al. (2016a, 2016b, 2018a, 2018b, 2021) and Wang et al. (2019) Samples

Object	EW(Hβ) (Å)	$\log_{10} R_{23}$	$\log_{10} O_{32}$	$\log_{10} O_{31}$	$\log_{10}$[O I]/Hβ
J003601+003307	160.469 ± 6.508	0.938 ± 0.023	1.116 ± 0.039	>2.618	<−1.167
J004743+015440	60.564 ± 1.136	0.955 ± 0.023	0.657 ± 0.026	>2.868	<−2.878
J011309+000223	38.730 ± 1.421	0.964 ± 0.075	0.356 ± 0.085	>2.349	<−1.331
J012217+052044	86.806 ± 3.110	0.942 ± 0.040	0.881 ± 0.046	>2.552	<−1.209
J012910+145935	69.484 ± 1.618	0.853 ± 0.026	0.343 ± 0.031	1.714 ± 0.088	−1.852 ± 0.088

(This table is available in its entirety in machine-readable form.)

Table 4
Properties Derived from the SDSS Optical Spectra for the Combined LzLCS and Izotov et al. (2016a, 2016b, 2018a, 2018b, 2021) and Wang et al. (2019) Samples

Object	$\log_{10}$SFR$_{H\beta}$	n_e (cm^{-3})	T_e (K)	$12 + \log_{10}\left(\frac{O}{H}\right)$
J003601+003307	1.184 ± 0.024	100	15770 ± 970	7.781 ± 0.037
J004743+015440	1.336 ± 0.024	1610 ± 150	13820 ± 850	8.290 ± 0.037
J011309+000223	0.699 ± 0.076	6590 ± 180	11640 ± 1060	8.329 ± 0.115
J012217+052044	0.971 ± 0.041	100	16220 ± 1760	7.799 ± 0.064
J012910+145935	1.125 ± 0.026	2600 ± 120	10000 ± 250	8.411 ± 0.044

(This table is available in its entirety in machine-readable form.)

Table 5
Properties Derived from the HST/COS G140L Spectra for the Combined LzLCS and Izotov et al. (2016a, 2016b, 2018a, 2018b, 2021) and Wang et al. (2019) Samples

Object	M_{1500}	r_{50} (kpc)	β_{1200}	$f_{1100} \times 10^{17}$ (erg s^{-1} cm^{-2} Å^{-1})	EW(Lyα) (Å)	$\log_{10}$SFR$_{f_{1100}}$ ($M_\odot$ yr^{-1})
J003601+003307	−18.527 ± 0.100	0.445 ± 0.148	−2.900 ± 0.328	$6.445^{+0.418}_{-0.381}$	93.900 ± 9.330	0.038 ± 0.028
J004743+015440	−20.732 ± 0.094	0.618 ± 0.145	−2.380 ± 0.298	$38.611^{+2.787}_{-2.507}$	41.526 ± 4.427	1.363 ± 0.031
J011309+000223	−20.268 ± 0.118	0.627 ± 0.133	−1.990 ± 0.253	$36.421^{+2.623}_{-3.649}$	31.291 ± 3.560	1.203 ± 0.031
J012217+052044	−20.143 ± 0.098	0.713 ± 0.151	−1.609 ± 0.274	$23.193^{+1.427}_{-1.595}$	70.616 ± 6.793	0.915 ± 0.027
J012910+145935	−20.439 ± 0.058	0.636 ± 0.127	−1.672 ± 0.205	$50.705^{+2.979}_{-3.600}$	39.593 ± 4.840	1.354 ± 0.026

(This table is available in its entirety in machine-readable form.)

Table 6
Properties Derived Jointly from HST/COS, and SDSS Data for the Combined LzLCS and Izotov et al. (2016a, 2016b, 2018a, 2018b, 2021) and Wang et al. (2019) Samples

Object	$f_{esc}^{Ly\alpha}$	$\log_{10}\Sigma_{SFR,H\beta}$	$\log_{10}\Sigma_{SFR,f_{1100}}$	$\log_{10} M_\star$
J003601+003307	0.116 ± 0.011	1.880 ± 0.146	0.249 ± 0.147	$8.754^{+0.444}_{-0.425}$
J004743+015440	0.194 ± 0.019	0.956 ± 0.105	0.945 ± 0.107	$9.203^{+0.439}_{-0.430}$
J011309+000223	0.398 ± 0.075	0.307 ± 0.119	0.860 ± 0.098	$9.111^{+0.438}_{-0.430}$
J012217+052044	0.594 ± 0.069	0.467 ± 0.100	0.417 ± 0.096	$8.762^{+0.448}_{-0.423}$
J012910+145935	0.193 ± 0.017	0.719 ± 0.091	0.965 ± 0.091	$9.154^{+0.583}_{-0.305}$

(This table is available in its entirety in machine-readable form.)

H I opacities than previously published surveys may have indicated.

To determine the spectral index β_{1200} of the rest-frame UV continuum, we fit the wide-extraction spectra using the affine-invariant Markov Chain Monte Carlo sampling software EMCEE (Foreman-Mackey et al. 2013) to sample the posterior of β_{1200}. We set a lower limit of 1050 Å in the rest frame to avoid the combined O VI λλ1032, 1038 Å, and C II λ1036 Å absorption features and mask the Galactic Lyα. We show the distribution of β_{1200} values in Figure 11. The LzLCS samples roughly the same range of $-2.5 < \beta_{1200} < -0.35$ as previous studies of local LCEs but with most galaxies concentrated at $\beta_{1200} = -1.6$. One exception, J131904+510309, exhibits substantial extinction in the UV–$E(B-V)_{UV} = 0.5$, $E(B-V)_{neb} = 0.42$—which results in $\beta_{1200} = 0.79$. While the LzLCS LCEs span a range in UV β comparable to that of previously published LCE candidates, our LCEs are, on average, redder, suggesting that LCEs can have a larger range of burst ages and/or dust content than previously found.

Because the flux at 1500 Å often falls outside the COS window for these redshifts, we also measure the continuum flux at 1100 Å as other studies have done (e.g., Wang et al. 2019). This spectral window is a reliably bright part of the starlight

Table 7
Measurements of the LyC

Object	λ_{LyC} [a] (Å)	Dark (counts)	Sky (counts)	Source (counts)	$P(>N\|B)$	$f_{LyC} \times 10^{17}$ [b] (erg s^{-1} cm^{-2} Å^{-1})
J003601+003307	860	62.388	19.298	13.314	0.066	<0.114
J004743+015440	860	12.438	6.664	25.898	1.305×10^{-7}	$1.557^{+0.457}_{-0.407}$
J011309+000223	890	8.970	6.471	20.559	2.282×10^{-6}	$1.445^{+0.490}_{-0.428}$
J012217+052044	850	34.209	5.945	34.845	3.045×10^{-7}	$1.118^{+0.292}_{-0.266}$
J012910+145935	890	11.290	9.734	2.237	0.266	<0.556

Notes.
[a] Rest-frame central wavelength of 20 Å LyC spectral window.
[b] LyC flux density corrected for MW extinction.
(This table is available in its entirety in machine-readable form.)

Table 8
Empirical $f_{\lambda LyC}/f_{\lambda 1100}$ and Absolute f_{esc}^{LyC} .

Object	f_{LyC}/f_{1100}	$f_{esc}^{LyC}(H\beta)$	$f_{esc}^{LyC}(UV)$
J003601+003307	<0.017	<0.005	<0.029
J004743+015440	$0.040^{+0.012}_{-0.010}$	$0.049^{+0.014}_{-0.012}$	$0.032^{+0.021}_{-0.003}$
J011309+000223	$0.040^{+0.013}_{-0.012}$	$0.123^{+0.042}_{-0.035}$	$0.007^{+0.016}_{-0.012}$
J012217+052044	$0.048^{+0.013}_{-0.012}$	$0.084^{+0.022}_{-0.019}$	$0.030^{+0.046}_{-0.016}$
J012910+145935	<0.011	<0.014	<0.007

Note. Derived from STARBURST99 using continuous star formation predictions and Hβ or the burst predictions fit to the HST/COS spectrum for the combined LzLCS and Izotov et al. (2016a, 2016b, 2018a, 2018b, 2021) and Wang et al. (2019) samples.
(This table is available in its entirety in machine-readable form.)

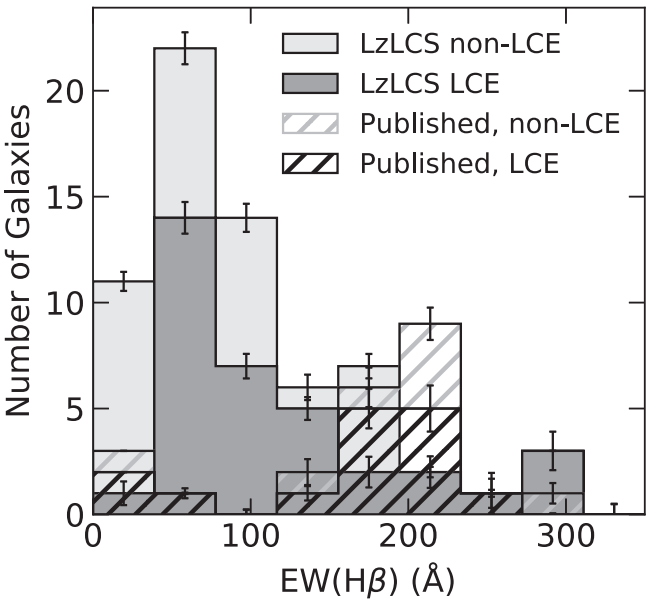

Figure 6. Distribution of rest-frame Hβ equivalent width (EW) values for galaxies in the LzLCS (solid) with detected LyC (dark gray) and undetected LyC (light gray). For comparison, we include the EWs for LCE candidates with published HST/COS spectra (hatched) with detected LyC (black) and undetected LyC (gray). Error bars represent the 1σ Poisson binomial uncertainty in each histogram bin.

continuum that avoids the aforementioned absorption features spanning 1030–1040 Å. We take $F(1100)$ to be the average flux from 1090–1110 Å, the same width as the LyC flux for consistency. At our sample's redshifts, this choice also serves to eliminate potential contamination of $F(1100)$ by telluric O I λ1304 emission.

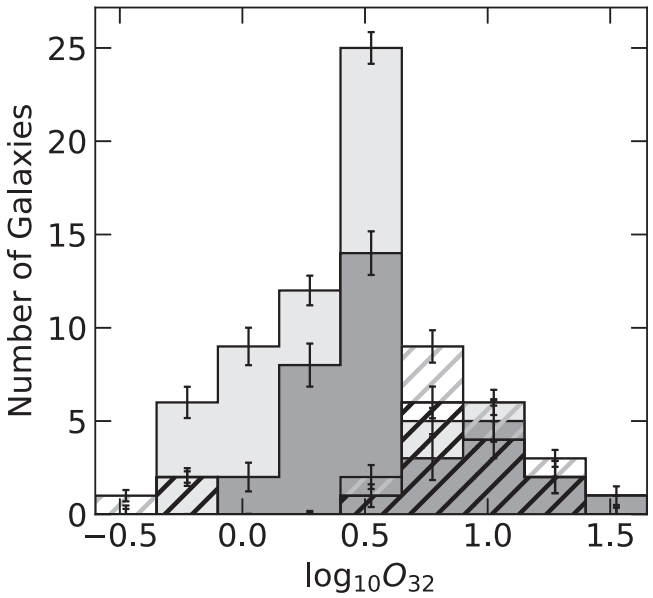

Figure 7. The same as Figure 6 but for [O III]λ5007/[O II]λ3727, 29 $= O_{32}$.

5.5. UV Spectral Modeling

Following Chisholm et al. (2019), we estimate stellar $E(B-V)$ values and f_{esc}^{LyC} by comparing our data with a library of synthetic spectra compiled from STARBURST99 models (Leitherer et al. 2010) for nonrotating stars and nebular continuum modeled by CLOUDY (Ferland et al. 2013). These models are fit to the continua with scaling factors multiplied by the Reddy et al. (2016) extinction law with reddening as an additional free parameter. Our reference library contains 40 synthetic spectra for simple stellar populations spanning 10 burst ages (1, 2, 3, 4, 5, 8, 10, 15, 20, and 40 Myr) and four metallicities (0.05, 0.2, 0.4, and 1 $Z_\odot$). These are combined allowing for multiple generations of star formation with metallicity as a free parameter (Saldana-Lopez et al. 2022). Fits are performed in the rest frame after convolving model spectra by a Gaussian kernel to the COS spectral resolution. We discuss the derivation of f_{esc}^{LyC} further in Section 6.

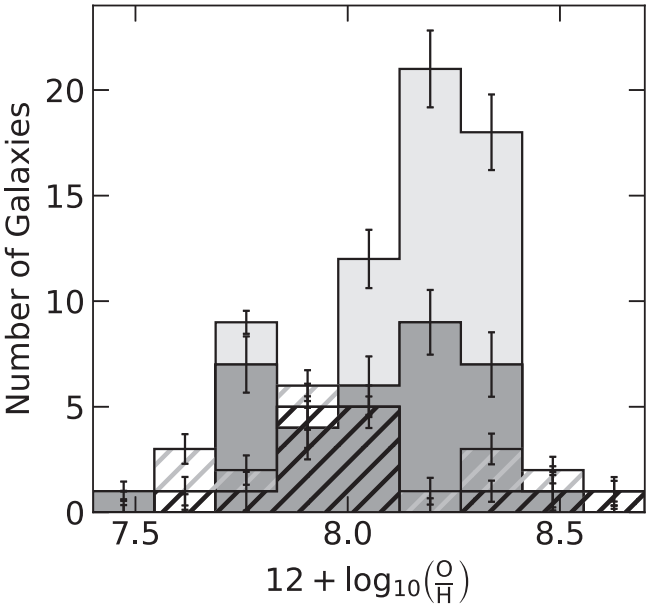

Figure 8. The same as Figure 6 but for $12 + \log_{10}(O/H)$.

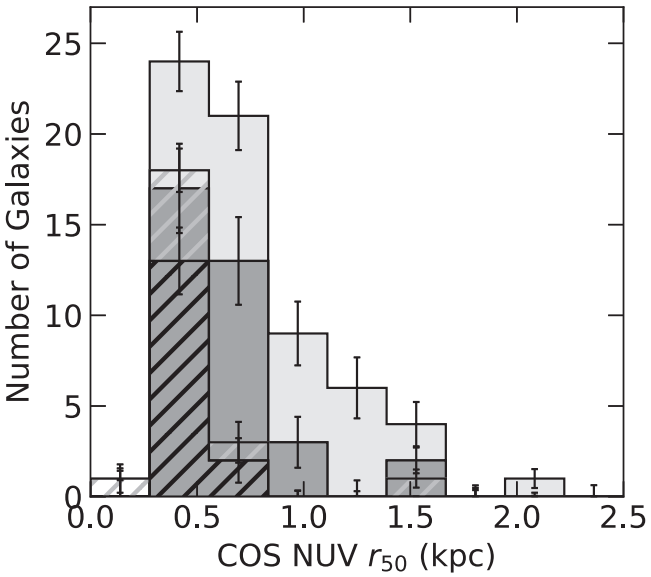

Figure 9. The same as Figure 6 but for r_{50}.

5.6. Star Formation Rate Surface Density and Stellar Mass

We convert the observed properties into an SFR surface density, Σ_{SFR}, assuming the Hβ and FUV SFR calibrations from Kennicutt & Evans (2012) and dividing by $2\pi r^2_{50,NUV}$ following Naidu et al. (2020). We note that these SFR indicators using Hβ and UV luminosities are based on standard calibrations rather than tailored to the detailed properties (e.g., metallicity) of our sample. Thus, these SFRs are more representative of the Hβ and FUV luminosities than the true SFR. Figure 12 shows that the LzLCS spans a much wider range in Σ_{SFR} than previous studies. While many LzLCS LCEs exhibit $\Sigma_{SFR} > 10\,M_\odot$ yr^{-1} like their published LCE counterparts, many LzLCS LCEs have much lower Σ_{SFR}. Since the LzLCS LCEs' half-light radii are similar to those of published LCEs, the difference in LCE Σ_{SFR} is a distinction in SFR, suggesting concentration is more important than SFR for LyC escape.

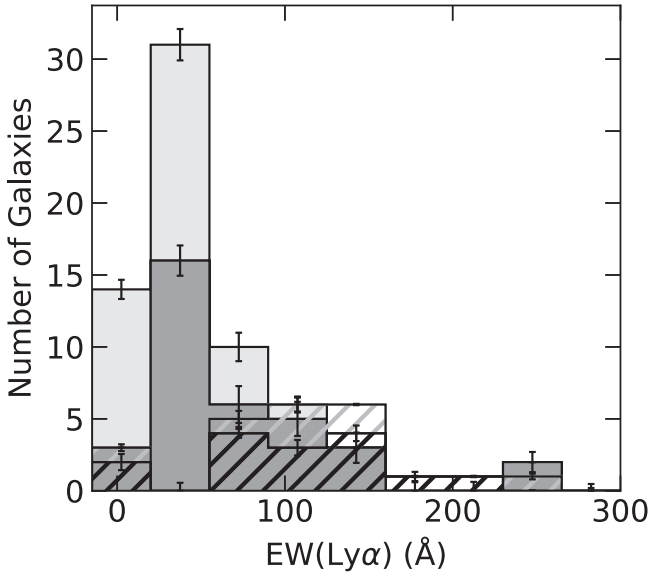

Figure 10. The same as Figure 6 but for rest-frame Lyα EW.

Stellar masses, $M_\star$, are determined by using the stellar population inference code PROSPECTOR (Leja et al. 2017; Johnson et al. 2019) to fit aperture-matched photometry from SDSS and GALEX assuming a nonparametric star formation history, a Kroupa (2001) initial mass function, CLOUDY photoionization models, and a Calzetti (2001) dust attenuation curve (Z. Ji et al. 2022, in preparation; see also M. J. Rutkowski et al. 2022, in preparation), noting that the inferred stellar mass changes negligibly if adopting the Reddy et al. (2016) extinction law instead. As shown in Figure 13, $M_\star$ ranges from $10^{8.25}$ to $10^{10.75}$ $M_\odot$ with half of the sample having $M_\star < 10^9$ $M_\odot$. The LzLCS LCEs are primarily dwarf galaxies but do persist up to much higher-mass ($M_\star > 10^{10}$ $M_\odot$) galaxies. While the distribution of LCEs suggests that dwarf galaxies dominate the LCE population, higher-mass galaxies can still be LCEs.

We use these stellar masses to compute the specific star formation rate, $\mathrm{sSFR} = \mathrm{SFR}_{H\beta}/M_\star$.

5.7. Lyα Escape Fraction

Using the temperatures and densities derived from the optical emission lines, we compute the Case B emissivities for Lyα and Hβ from the PYNEB grid of recombination coefficients from Storey & Hummer (1995). We correct Hβ for both Galactic and internal extinction and use the ratio of Lyα to Hβ emissivities to infer the intrinsic Lyα flux. We then use the observed Lyα flux, corrected for Galactic extinction, to calculate the fraction of Lyα photons, $f_{esc}^{Ly\alpha}$, which escape the host galaxy. Uncertainties in the $f_{esc}^{Ly\alpha}$ are determined using Monte Carlo sampling of the grid of Case B emissivities from the uncertainties in temperature and density. We show the distribution of $f_{esc}^{Ly\alpha}$ values in Figure 14. While the LzLCS samples roughly the same range of $f_{esc}^{Ly\alpha}$ in [0, 0.6] as previous studies, half of the sample exhibits low (<16%) Lyα escape. This concentration at low $f_{esc}^{Ly\alpha}$ suggests a high H I column along the line of sight in many of the LzLCS galaxies (e.g., Verhamme et al. 2015).

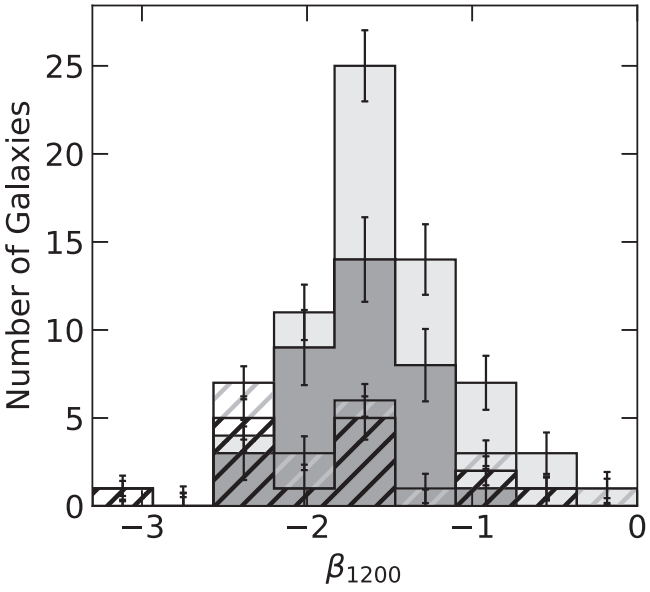

Figure 11. The same as Figure 6 but for β_{1200}.

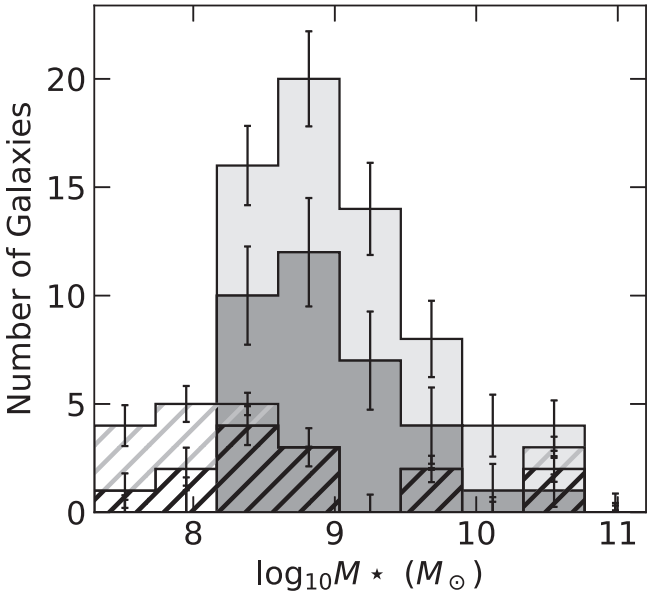

Figure 13. The same as Figure 6 but for $M_\star$.

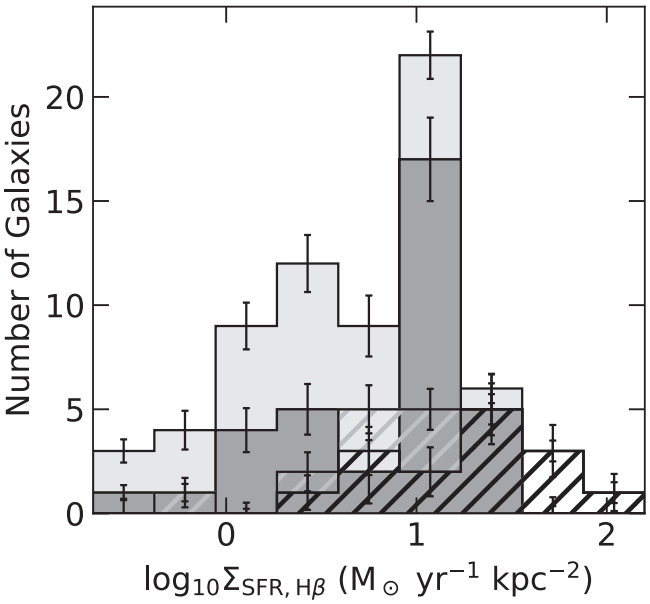

Figure 12. The same as Figure 6 but for Σ_{SFR} derived from Hβ.

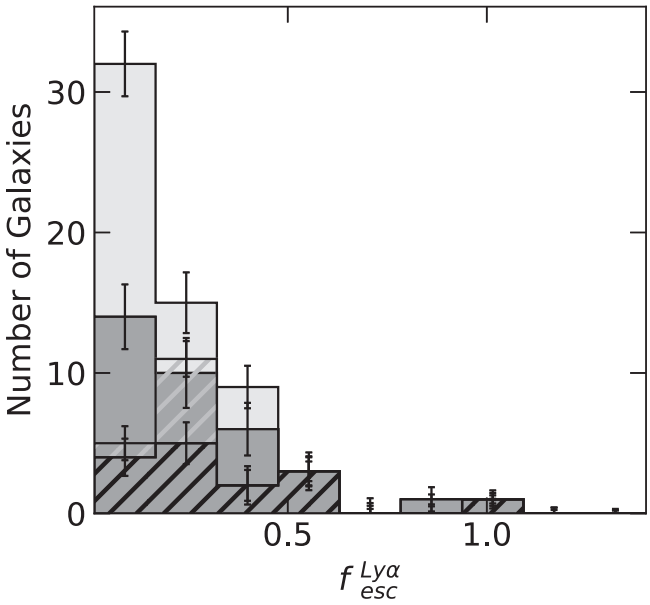

Figure 14. The same as Figure 6 but for $f^{Ly\alpha}_{esc}$.

As demonstrated in Figure 14, two objects exhibit atypically high $f^{Ly\alpha}_{esc}$: J081112+414146 and J164849+495751. These galaxies also have Hα/Hβ and Hγ/Hβ decrements that are not permitted by traditional Case B limits of $\geqslant 2.747$ and $\leqslant 0.475$, respectively. This inconsistency most likely indicates that the Balmer lines in SDSS spectra are problematic. Alternatively, such high $f^{Ly\alpha}_{esc}$ values may indicate collisional excitation of the H I $n = 2$ state in galactic winds or a hot diffuse halo (e.g., Carr et al. 2021) or excess Lyα scattered into the line of sight (e.g., Giavalisco et al. 1996). Excepting these two extreme cases, the LzLCS LCEs tend to have $f^{Ly\alpha}_{esc} < 0.5$ like their published counterparts. However, the LzLCS non-LCEs tend to have much lower $f^{Ly\alpha}_{esc}$ (< 0.15). Such $f^{Ly\alpha}_{esc}$ values demonstrate that the LzLCS more robustly samples the LCE population at high H I column densities than previous studies and even suggest LyC photons can escape even when a substantial amount of neutral gas is present.

5.8. Lyα Peak Velocity Separation

The G140L resolution is insufficient to resolve the red and blue peaks of the Lyα profile. However, seven targets from the LzLCS have existing archival G160M COS spectra in which the two peaks are resolved. We obtain measurements of the velocity separation v_{sep} of these peaks from Henry et al. (2015), Yang et al. (2017), and Orlitová et al. (2018) and compare them to peak separations for published LCEs from Verhamme et al. (2017) and Izotov et al. (2018b) in Figure 15. While the number of LzLCS galaxies with measured v_{sep} is small, the LCEs in our sample have Lyα peak separations larger than the characteristic value for published LCEs. This difference

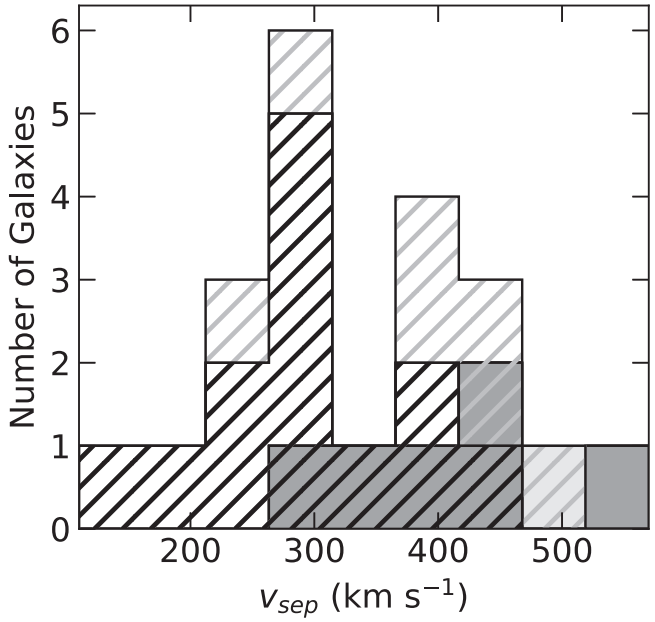

Figure 15. The same as Figure 6 but for the velocity separation of the blue and red peaks of the Lyα profile. No error bars are shown as insufficient uncertainties are reported in the literature.

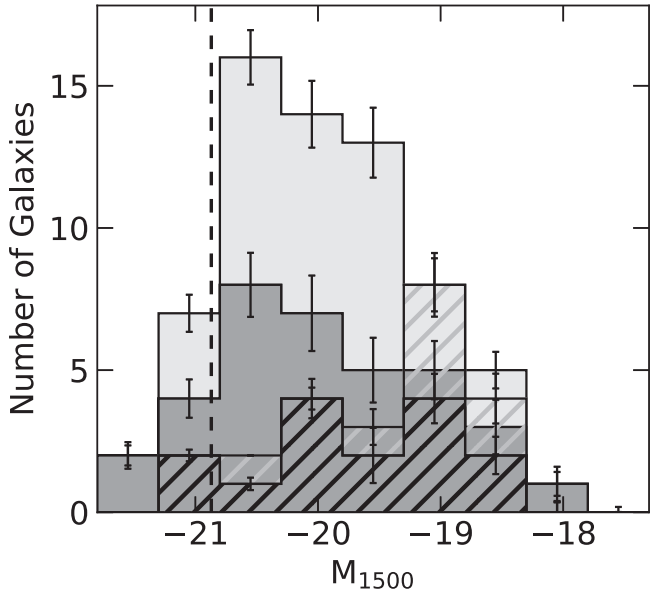

Figure 16. The same as Figure 6 but for M_{1500}. The dashed line indicates the characteristic $M^*_{1600} = -20.87$ at $z = 7$ (Bouwens et al. 2015).

indicates a larger H I column density in the LzLCS LCEs than in published LCEs, which may suggest LyC escape can occur in a variety of ISM geometries. However, the lack of $v_{\rm sep}$ measurements prevents further insight.

5.9. UV Magnitudes

We compute the absolute UV magnitude at 1500 Å (M_{1500}) from the STARBURST99 templates best fit to the COS spectra after correcting for Galactic (but *not* internal) extinction. These magnitudes are computed by summing the template flux density over a 20 Å boxcar window and converting to absolute AB magnitude using the luminosity distance derived from the spectroscopic redshift.

We show the COS UV magnitudes in Figure 16, finding $M_{1500} \in [-22, -17]$. Figure 16 indicates that the younger stellar populations in many LzLCS galaxies are, like their published counterparts, fainter than the characteristic $M^\star$. However, the LCEs in LzLCS span a wider range in M_{1500} than the published LCEs, indicating that more luminous galaxies can also be LCEs.

6. LyC Escape Fraction

We use three estimates of the LyC escape fraction, $f_{\rm esc}^{\rm LyC}$: (1) the $F_{\lambda \rm LyC}/F_{\lambda 1100}$ flux ratio, (2) $f_{\rm esc}^{\rm LyC}$ derived from Hβ, and (3) $f_{\rm esc}^{\rm LyC}$ determined from fits to the UV continuum. Each independent metric allows us to assess possible systematics in $f_{\rm esc}^{\rm LyC}$, providing an additional constraint on how much the escape fraction depends on our assumptions about, e.g., star formation history, dust extinction, etc. The $F_{\lambda \rm LyC}/F_{\lambda 1100}$ flux ratio is an empirical proxy for $f_{\rm esc}^{\rm LyC}$ (see Wang et al. 2019). While less direct than $f_{\rm esc}^{\rm LyC}$, $F_{\lambda \rm LyC}/F_{\lambda 1100}$ is free of any assumptions about stellar populations or dust. However, this flux ratio depends implicitly on extinction, burst age, and metallicity, making a direct interpretation less meaningful. Values for this flux ratio span 0.0 to 0.328 with a median of 0.023.

6.1. Hβ f_{esc}^{LyC}

To estimate the absolute $f_{\rm esc}^{\rm LyC}$, we use the extinction-corrected flux and rest-frame EW of Hβ to infer the LyC absorbed by the ISM in the galaxy as described by Izotov et al. (2016b, 2018a). This approach assumes that the extinction-corrected Hβ flux is a proxy for the total number of ionizing photons absorbed by the nebula (e.g., Osterbrock & Ferland 2006). The conversion between the total ionizing photon flux and the LyC flux at a particular wavelength depends on the stellar population age. The Hβ EW yields the burst age for an assumed star formation history. Use of the Hβ EW is necessary to select the appropriate model $F_{\rm H\beta}^{\rm mod}/F_{\lambda \rm LyC}^{\rm mod}$ independent of the UV spectral energy distribution (SED) fits. Here, the $F_{\rm H\beta}^{\rm mod}/F_{\lambda \rm LyC}^{\rm mod}$ ratio accounts for the shape of the LyC by tracing the amount of ionizing flux that falls within the 20 Å bin over which the LyC flux is measured. Because the ionization cross section of H I is proportional to λ^3, the emergent flux increases with decreasing LyC wavelength for a fixed escape fraction. We calculate the synthetic LyC flux in the 20 Å bins used to measure the LyC in the COS spectra, matching the model and observed wavelength bins.

To obtain model LyC and Hβ values for deriving $f_{\rm esc}^{\rm LyC}$, we consider two sets of population models, each with two different star formation histories. To predict LyC fluxes and Hβ properties, we use STARBURST99 models (Leitherer et al. 1999, 2014) and BPASS models (Stanway & Eldridge 2018) assuming either an instantaneous burst or continuous star formation. Model ages span from 0.1 to 500 Myr while metallicities range from $Z = 0.001$ to 0.04. For the STARBURST99 and BPASS models, we assume Kroupa (2001) and Chabrier (2003) initial mass functions, respectively, with mass ranges from 0.1–100 $M_\odot$ for both sets of models. In all cases, the shape of the relation changes as a function of stellar metallicity (see Figure 17), meaning there is no single function from which to infer the absorbed LyC flux. To select the appropriate sequence, we take advantage of our $12 + \log_{10}$(O/H) abundance estimate derived in Section 5.2, assuming that the gas and stellar metallicities are comparable

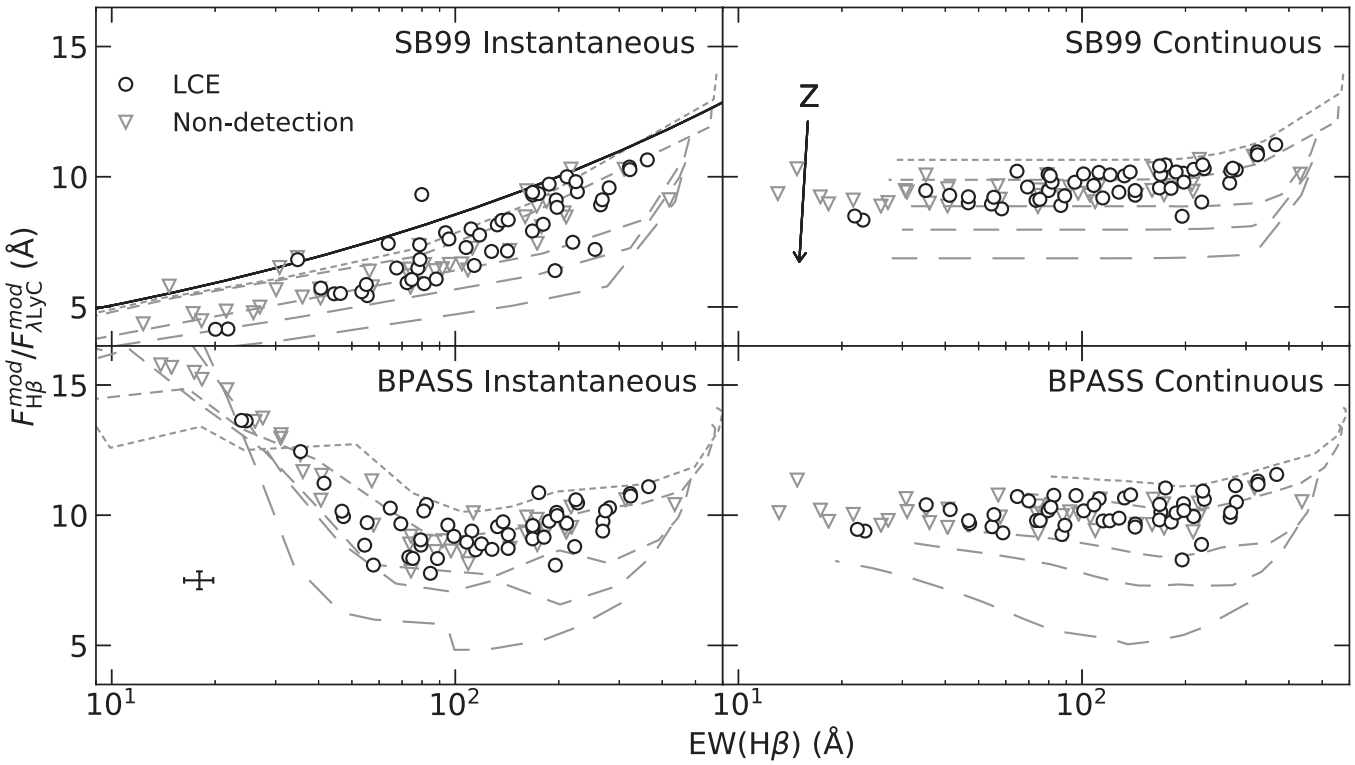

Figure 17. $F_{H\beta}^{mod}/F_{\lambda 900}^{mod}$ ratio predicted by instantaneous (left) and continuous (right) star formation histories from STARBURST99 (top) and BPASS (bottom) models for $f_{esc}^{LyC} = 0$ as a function of Hβ EW for a range of metallicities. Metallicity increases with increasing dash length over the interval $Z = [0.001, 0.04]$, as shown by the arrow in the top-right panel. The change in $F_{H\beta}/F_{\lambda LyC}$ with metallicity is due to the softening of stellar SEDs with increasing metallicity. The solid black line (top-left panel) indicates the Izotov et al. (2016b) relation. Symbols represent the inferred $F_{H\beta}/F_{\lambda LyC}$ for $f_{esc}^{LyC} = 0$ for LCEs (circles) and nondetections (open triangles) implied by the measured $F_{\lambda LyC}$, Hβ, $12 + \log_{10}\left(\frac{O}{H}\right)$, and f_{esc}^{LyC} for each set of models. Median uncertainties are shown in the bottom-left panel, increased by a factor of three for visualization.

since the stars have recently formed and have not yet further enriched the ISM. While at high redshift, α enhancement may affect the scaling of oxygen to total metallicity; however, Izotov et al. (2011) found that GPs have Fe/O ratios comparable to those of other low-redshift dwarf galaxies and that dust depletion sufficiently explains any apparent gas-phase α excess relative to iron. Thus, scaling the total metallicity by the relative oxygen abundance is appropriate for the combined sample.

We then interpolate over the grid of $F_{H\beta}/F_{\lambda LyC}$ from the stellar population models to obtain the predicted intrinsic flux ratio versus Hβ EW for the given galaxy's metallicity. As in Izotov et al. (2016b), we take the LyC flux $F_{\lambda LyC}^{abs}$ implied by the Hβ flux to be the absorbed LyC flux such that the f_{esc}^{LyC} is

$$f_{esc}^{LyC}(H\beta) = \frac{F_{\lambda LyC}^{obs}}{F_{\lambda LyC}^{obs} + F_{\lambda LyC}^{abs}} = \frac{F_{\lambda LyC}^{obs}}{F_{\lambda LyC}^{mod}}. \quad (3)$$

This relation is only an initial estimate as the Hβ EW, the burst age indicator used to infer $F_{H\beta}^{mod}/F_{\lambda LyC}^{mod}$, is in fact affected by LyC escape, meaning that Hβ EW must be corrected for f_{esc} in order to yield the appropriate flux ratio (e.g., Izotov et al. 2018b). Using the f_{esc}^{LyC} calculated from the uncorrected value as the initial condition, we iteratively correct Hβ EW and recompute f_{esc} until converging on a value of f_{esc}^{LyC}, typically within 10 or fewer iterations. Uncertainties in f_{esc}^{LyC} are estimated by Monte Carlo simulation, sampling the uncertainties in Hβ flux and EW, LyC flux, and $12 + \log_{10}$(O/H) and recalculating f_{esc}^{LyC} 10^4 times.

As is evident in Figure 17, the STARBURST99 models reproduce the Izotov et al. (2016b) relation between Hβ EW and the $F_{H\beta}/F_{\lambda LyC}$ flux ratio for an instantaneous starburst of 10% solar metallicity (Figure 17, top-left panel). However, our results indicate that using the Izotov et al. (2016b) prescription will consistently yield higher $F_{H\beta}/F_{\lambda LyC}$ and thus overestimate f_{esc}^{LyC} for an instantaneous burst. We also take into account the effects of binary star evolution by considering the BPASS model (Stanway & Eldridge 2018). This model increases the ionizing photon budget by an amount comparable to that of the continuous starburst (Figure 17, bottom-left panel). Continuous STARBURST99 and BPASS models predict $F_{H\beta}/F_{\lambda LyC}$ values higher than those of the STARBURST99 instantaneous burst models (Figure 17, top- and bottom-right panels), with the difference increasing as Hβ EW decreases due to subsequent generations of young stars.

Using the Hβ line with the STARBURST99 and BPASS continuous star formation models yields f_{esc}^{LyC} values ranging from 0% to 20% for the LzLCS sample and from 0% to 45% for the published LCEs. Fifteen of the LzLCS LCEs and nine of the published LCEs have cosmologically relevant values of $f_{esc}^{LyC} > 0.05$. The BPASS instantaneous burst models yield similar results, with a median difference in f_{esc}^{LyC} of $\approx 0.001\%$. The f_{esc}^{LyC} values derived from STARBURST99 instantaneous star formation models diverge from the BPASS and STARBURST99 f_{esc}^{LyC} with increasing burst age. We illustrate this effect in Figure 18 by comparing the difference in f_{esc}^{LyC} to the Hβ EW. For the youngest bursts, the difference is negligible because the early O stars dominate the LyC and optical continuum in every

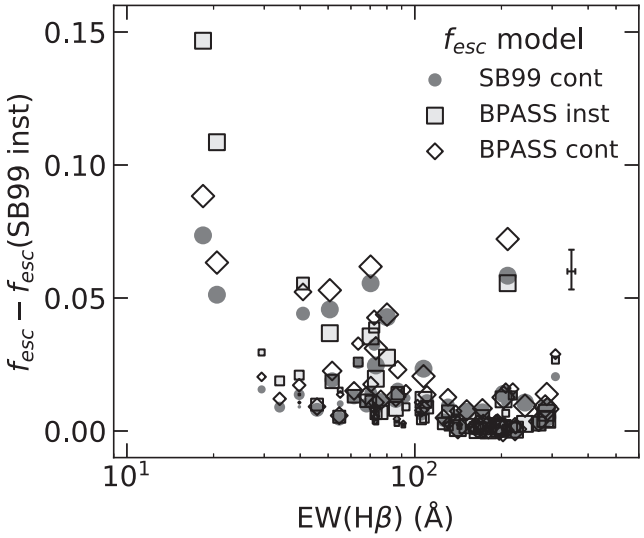

Figure 18. Difference between f_{esc}^{LyC} calculated from BPASS instantaneous (open diamonds) and continuous (light gray squares) star formation or from STARBURST99 continuous star formation (dark gray circles) models and f_{esc}^{LyC} calculated using STARBURST99 instantaneous star formation models as compared to Hβ EW for f_{esc}^{LyC} derived from Hβ for the combined LzLCS and published samples. Symbol size corresponds to the LyC detection significance. Characteristic uncertainties are shown on the right. Increasing scatter with decreasing Hβ EW indicates the increasing effect of assumptions about star formation history on the inferred f_{esc}^{LyC}.

scenario; however, the effects of continuously forming new O and B stars or accretion onto stripped stars in binary star systems can amplify f_{esc}^{LyC} by as much as a factor of two or three, respectively, at later burst ages.

6.2. UV SED f_{esc}^{LyC}

To determine f_{esc}^{LyC} from the UV continuum fits, we compute the ratio of the measured LyC flux to the intrinsic (unreddened) LyC flux implied by the best-fit STARBURST99 templates. We obtain the intrinsic LyC flux by using the low-resolution STARBURST99 bases, summing the model flux in the same spectral window used to measure the LyC in the COS spectrum. The UV escape fraction is then obtained by

$$f_{esc}^{LyC}(\mathrm{UV}) = \frac{F_{\lambda LyC}^{obs}}{F_{\lambda LyC}^{fit}}. \quad (4)$$

This yields a range of f_{esc}^{LyC} from 0% to 50% with nine of the LzLCS LCEs having $f_{esc}^{LyC} > 0.05$. While the uncertainties for the UV f_{esc}^{LyC} are higher due to the S/N of the COS spectrum, this approach is less sensitive to the presence of older stellar populations than Hβ because the FUV continuum is only sensitive to the youngest stars.

6.3. Comparison of f_{esc}^{LyC} Results

In Figure 19, we show that the UV and Hβ methods typically agree to within ∼0.5 dex, which we confirm by calculating the rms ratio of the two f_{esc}^{LyC} values. Even the strongest LCEs exhibit this scatter, indicating the persistence of systematic uncertainty across a dynamic range of escape fractions. The UV f_{esc}^{LyC} values are consistently higher at high values of $F_{\lambda LyC}/F_{\lambda 1100}$. While both approaches to deriving f_{esc}^{LyC} depend on assumptions, the consistency between all three measures of LyC escape gives us confidence in assessing the relevance of different galaxies to reionization. Despite the effects of extinction and stellar populations implicit to the measured $F_{\lambda LyC}/F_{\lambda 1100}$, we show in Figure 19 that f_{esc}^{LyC} correlates well with it, indicating this flux ratio is a rough proxy for f_{esc}^{LyC}. Of all of the Hβ f_{esc}^{LyC} estimates, the STARBURST99 continuous star formation models yield f_{esc}^{LyC} values most consistent with the UV f_{esc}^{LyC}. This agreement suggests the UV and continuous Hβ EW star formation histories are most comparable, although discrepancies still persist between the two. We find that the observed $F_{\lambda LyC}/F_{\lambda 1100}$ are best predicted by the continuous star formation models. Thus, we proceed with f_{esc}^{LyC} derived using the continuous star formation models in subsequent analysis.

While the UV-fit f_{esc}^{LyC} tends to be higher at high $F_{\lambda LyC}/F_{\lambda 1100}$, only nine LzLCS targets have significantly high f_{esc}^{LyC} (>0.05). Despite lower maximum f_{esc}^{LyC} values, Hβ yields 15 objects with high f_{esc}^{LyC}. In our remeasurement of f_{esc}^{LyC} for published HST/COS LyC observations, we find 13 have high f_{esc}^{LyC} from fits to the UV continuum, and 14 have high f_{esc}^{LyC} from Hβ. Thus, through the LzLCS, we have roughly doubled the number of known LCEs with cosmologically significant f_{esc}^{LyC} ($\gtrsim 5$ %), demonstrating the immense scientific value of the LzLCS program.

7. Conclusion

We present the Low-redshift Lyman Continuum Survey, the largest search for LCEs in the low-redshift ($z \sim 0.3$) universe. With careful processing of HST/COS spectra, we measure the LyC in 66 candidate LCEs, detecting flux with >97.725% significance from 35 galaxies in the sample. The LzLCS nearly triples the number of known local LCEs.

From UV and optical spectra and UV photometry, we characterize the global properties of the LzLCS galaxies. The sample contains low metallicity galaxies with direct-method oxygen abundances ranging from $12 + \log_{10}(\mathrm{O/H}) = 7.5$ to 8.5, a much broader range than previously published LCEs. Stellar masses span $M_\star = 10^8$ to 10^{10} $M_\odot$ with the UV half-light radii ranging from 0.3 to 2.25 kpc. The half-light radii, Σ_{SFR}, and *sSFR* imply highly concentrated star formation. Hβ EWs and O_{32} imply a range of starburst ages, ionization parameter, and/or optical depth effects. The LzLCS covers a wider range of properties than previously published low-redshift LCEs, demonstrating the ability of our survey to explore and test the heterogeneity of LCEs and f_{esc}^{LyC}.

From empirical methods and synthetic stellar population models, we derive escape fractions ranging from 0% to 50%. Although previous studies suggest f_{esc}^{LyC} derived by different methods agree (e.g., Izotov et al. 2016b, 2018b), the broader scope of the LzLCS demonstrates that f_{esc}^{LyC} estimates can be sensitive to assumptions about stellar populations and star formation history as well as the data used. Based on our assessment of different methods and related systematic uncertainties, the f_{esc}^{LyC} based on the UV starlight continuum is the most reliable because it is less sensitive to assumptions than the f_{esc}^{LyC} based on Hβ.

With the LzLCS, we have roughly doubled the number of local LCEs with cosmologically relevant LyC escape ($f_{esc}^{LyC} > 0.05$; e.g., Robertson et al. 2015) from 13 to 22 (or 14 to 29) using the UV (or Hβ) method. The LzLCS thus offers an unprecedented opportunity to investigate the conditions

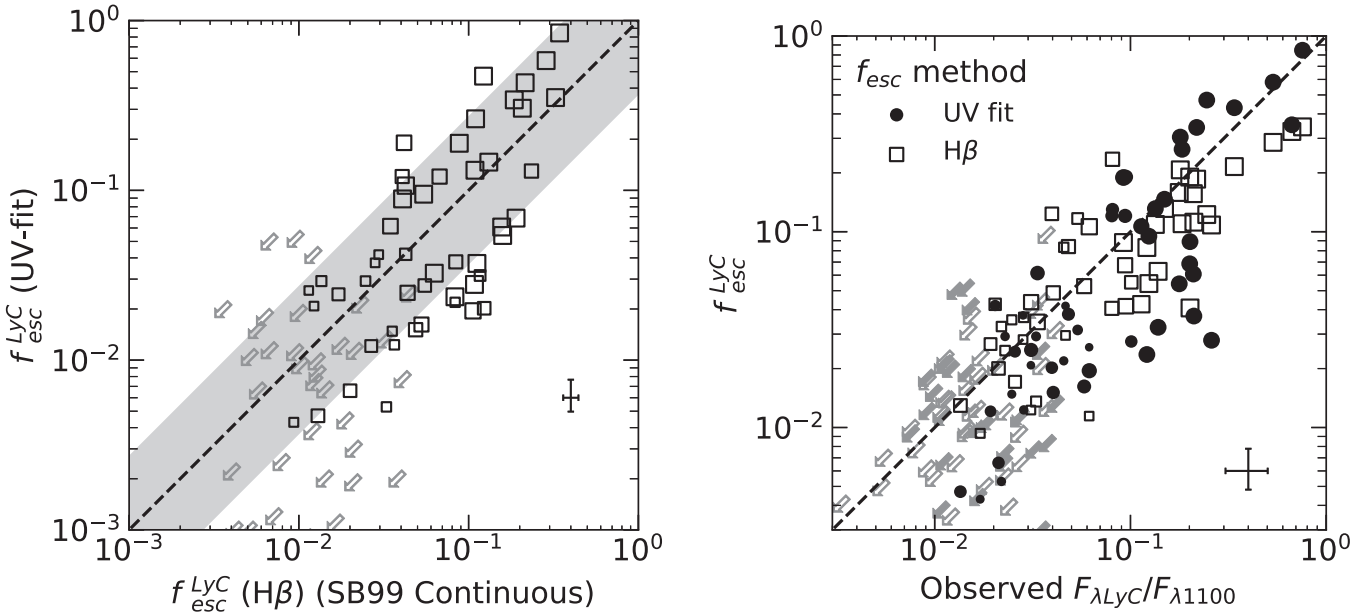

Figure 19. Top: f_{esc}^{LyC} derived from fitting the COS UV spectrum compared to f_{esc}^{LyC} derived from Hβ using the STARBURST99 continuous star formation models. The shaded region indicates the rms log difference of the two f_{esc}^{LyC} values. Bottom: comparison of f_{esc}^{LyC} with $F_{\lambda LyC}/F_{\lambda 1100}$ for the combined sample of LzLCS and published LCEs. Open symbols represent f_{esc}^{LyC} derived from Hβ using the STARBURST99 continuous star formation models, while filled symbols represent f_{esc}^{LyC} derived from fits to the UV continuum. In both figures, symbol size corresponds to the LyC detection significance, and gray arrows indicate upper limits on f_{esc}^{LyC}. Error bars in the bottom right indicate the median uncertainty for objects with detected LyC ($P(>N|B) < 0.02275$). The dashed line is 1:1 agreement.

related to LyC escape in galaxies, the results of which may be extended to the Epoch of Reionization.

We evaluate LCE and f_{esc}^{LyC} diagnostics in companion papers (Wang et al. 2021; Flury et al. 2022). We also analyze the UV absorption lines (Saldana-Lopez et al. 2022) and SED parameters (Z. Ji et al. 2022, in preparation) of LCEs and nonemitters. Additional planned work includes investigation of the shape of the LyC and the Lyman break, feedback and gas dynamics, neutral and low-ionization gas covering fractions, and photoionization modeling to further understand the ISM conditions and physical mechanisms of escaping LyC.

We thank the anonymous referee for feedback that improved the clarity of this paper.

Support for this work was provided by NASA through grant No. HST-GO-15626 from the Space Telescope Science Institute. Additional work was based on observations made with the NASA/ESA Hubble Space Telescope, obtained from the data archive at the Space Telescope Science Institute from HST proposals 13744, 14635, 15341, and 15639. STScI is operated by the Association of Universities for Research in Astronomy, Inc. under NASA contract NAS 5-26555.

Funding for the Sloan Digital Sky Survey IV has been provided by the Alfred P. Sloan Foundation, the U.S. Department of Energy Office of Science, and the Participating Institutions. SDSS-IV acknowledges support and resources from the Center for High Performance Computing at the University of Utah. The SDSS website is www.sdss.org. SDSS-IV is managed by the Astrophysical Research Consortium for the Participating Institutions of the SDSS Collaboration.

R.A. acknowledges support from ANID Fondecyt Regular 1202007.

Software: astropy (Astropy Collaboration et al. 2013, 2018), BPASS (Stanway & Eldridge 2018), CALCOS, CLOUDY (Ferland et al. 2013), EMCEE (Foreman-Mackey et al. 2013), FAINTCOS (Worseck et al. 2016; Makan et al. 2021), MATPLOTLIB (Hunter 2007), NUMPY (van der Walt et al. 2011), PROSPECTOR (Leja et al. 2017; Johnson et al. 2019), PYNEB (Luridiana et al. 2015), SCIPY (Virtanen et al. 2020), STARBURST99 (Leitherer et al. 1999, 2010, 2014).

ORCID iDs

Sophia R. Flury https://orcid.org/0000-0002-0159-2613
Anne E. Jaskot https://orcid.org/0000-0002-6790-5125
Harry C. Ferguson https://orcid.org/0000-0001-7113-2738
Gábor Worseck https://orcid.org/0000-0003-0960-3580
Kirill Makan https://orcid.org/0000-0003-3157-1191
John Chisholm https://orcid.org/0000-0002-0302-2577
Alberto Saldana-Lopez https://orcid.org/0000-0001-8419-3062
Daniel Schaerer https://orcid.org/0000-0001-7144-7182
Stephan McCandliss https://orcid.org/0000-0003-0503-4667
Bingjie Wang https://orcid.org/0000-0001-9269-5046
N. M. Ford https://orcid.org/0000-0001-8921-3624
Timothy Heckman https://orcid.org/0000-0001-6670-6370
Zhiyuan Ji https://orcid.org/0000-0001-7673-2257
Mauro Giavalisco https://orcid.org/0000-0002-7831-8751
Ricardo Amorin https://orcid.org/0000-0001-5758-1000
Sanchayeeta Borthakur https://orcid.org/0000-0002-2724-8298
Cody Carr https://orcid.org/0000-0003-4166-2855
Marco Castellano https://orcid.org/0000-0001-9875-8263
Stefano Cristiani https://orcid.org/0000-0002-2115-5234
Stephane De Barros https://orcid.org/0000-0002-5877-8793
Mark Dickinson https://orcid.org/0000-0001-5414-5131
Steven L. Finkelstein https://orcid.org/0000-0001-8519-1130
Brian Fleming https://orcid.org/0000-0002-2129-0292
Fabio Fontanot https://orcid.org/0000-0003-4744-0188

Matthew Hayes https://orcid.org/0000-0001-8587-218X
Alaina Henry https://orcid.org/0000-0002-6586-4446
Genoveva Micheva https://orcid.org/0000-0003-4376-2841
M. S. Oey https://orcid.org/0000-0002-5808-1320
Goran Ostlin https://orcid.org/0000-0002-3005-1349
Casey Papovich https://orcid.org/0000-0001-7503-8482
Laura Pentericci https://orcid.org/0000-0001-8940-6768
Michael Rutkowski https://orcid.org/0000-0001-7016-5220
Paola Santini https://orcid.org/0000-0002-9334-8705
Claudia Scarlata https://orcid.org/0000-0002-9136-8876
Harry Teplitz https://orcid.org/0000-0002-7064-5424
Maxime Trebitsch https://orcid.org/0000-0002-6849-5375
Eros Vanzella https://orcid.org/0000-0002-5057-135X
Xinfeng Xu https://orcid.org/0000-0002-9217-7051

References

Amorín, R., Pérez-Montero, E., Vílchez, J. M., & Papaderos, P. 2012, ApJ, 749, 185
Amorín, R. O., Pérez-Montero, E., & Vílchez, J. M. 2010, ApJL, 715, L128
Astropy Collaboration, Robitaille, T. P., Tollerud, E. J., et al. 2013, A&A, 558, A33
Astropy Collaboration, Price-Whelan, A. M., SipHocz, B. M., et al. 2018, AJ, 156, 123
Baldwin, J. A., Phillips, M. M., & Terlevich, R. 1981, PASP, 93, 5
Becker, G. D., D'Aloisio, A., Christenson, H. M., et al. 2021, MNRAS, 508, 1853
Becker, R. H., Fan, X., White, R. L., et al. 2001, AJ, 122, 2850
Bergvall, N., Leitet, E., Zackrisson, E., & Marquart, T. 2013, A&A, 554, A38
Bian, F., Fan, X., McGreer, I., Cai, Z., & Jiang, L. 2017, ApJL, 837, L12
Blanton, M. R., Bershady, M. A., Abolfathi, B., et al. 2017, AJ, 154, 28
Borthakur, S., Heckman, T. M., Leitherer, C., & Overzier, R. A. 2014, Sci, 346, 216
Bouwens, R. J., Smit, R., Labbé, I., et al. 2016, ApJ, 831, 176
Bouwens, R. J., Illingworth, G. D., Oesch, P. A., et al. 2015, ApJ, 803, 34
Calzetti, D. 2001, PASP, 113, 1449
Cardamone, C., Schawinski, K., Sarzi, M., et al. 2009, MNRAS, 399, 1191
Cardelli, J. A., Clayton, G. C., & Mathis, J. S. 1989, ApJ, 345, 245
Carr, C., Scarlata, C., Henry, A., & Panagia, N. 2021, ApJ, 906, 104
Chabrier, G. 2003, PASP, 115, 763
Chisholm, J., Orlitová, I., Schaerer, D., et al. 2017, A&A, 605, A67
Chisholm, J., Rigby, J. R., Bayliss, M., et al. 2019, ApJ, 882, 182
Clarke, C., & Oey, M. S. 2002, MNRAS, 337, 1299
Curti, M., Cresci, G., Mannucci, F., et al. 2017, MNRAS, 465, 1384
Dayal, P., Volonteri, M., Choudhury, T. R., et al. 2020, MNRAS, 495, 3065
de Barros, S., Vanzella, E., Amorín, R., et al. 2016, A&A, 585, A51
Deharveng, J. M., Buat, V., Le Brun, V., et al. 2001, A&A, 375, 805
Fan, X., Strauss, M. A., Becker, R. H., et al. 2006, AJ, 132, 117
Feldman, G. J., & Cousins, R. D. 1998, PhRvD, 57, 3873
Ferland, G. J., Porter, R. L., van Hoof, P. A. M., et al. 2013, RMxAA, 49, 137
Finkelstein, S. L., Ryan, R. E. J., Papovich, C., et al. 2015, ApJ, 810, 71
Finkelstein, S. L., D'Aloisio, A., Paardekooper, J.-P., et al. 2019, ApJ, 879, 36
Fitzpatrick, E. L. 1999, PASP, 111, 63
Fletcher, T. J., Tang, M., Robertson, B. E., et al. 2019, ApJ, 878, 87
Flury, S. R., Jaskot, A. E., Ferguson, H. C., et al. 2022, ApJ, in press (arXiv:2203.15649)
Flury, S. R., & Moran, E. C. 2020, MNRAS, 496, 2191
Foreman-Mackey, D., Hogg, D. W., Lang, D., & Goodman, J. 2013, PASP, 125, 306
Giavalisco, M., Koratkar, A., & Calzetti, D. 1996, ApJ, 466, 831
Gordon, K. D., Clayton, G. C., Misselt, K. A., Land olt, A. U., & Wolff, M. J. 2003, ApJ, 594, 279
Green, G. M., Schlafly, E. F., Finkbeiner, D., et al. 2018, MNRAS, 478, 651
Green, J. C., Froning, C. S., Osterman, S., et al. 2012, ApJ, 744, 60
Guaita, L., Melinder, J., Hayes, M., et al. 2015, A&A, 576, A51
Gunn, J. E., & Peterson, B. A. 1965, ApJ, 142, 1633
Hayes, M., Östlin, G., Schaerer, D., et al. 2013, ApJL, 765, L27
Heckman, T. M., Sembach, K. R., Meurer, G. R., et al. 2001, ApJ, 558, 56
Henry, A., Scarlata, C., Martin, C. L., & Erb, D. 2015, ApJ, 809, 19
Hunter, J. D. 2007, CSE, 9, 90
Inoue, A. K., Shimizu, I., Iwata, I., & Tanaka, M. 2014, MNRAS, 442, 1805
Izotov, Y. I., Guseva, N. G., Fricke, K. J., Henkel, C., & Schaerer, D. 2017, MNRAS, 467, 4118
Izotov, Y. I., Guseva, N. G., & Thuan, T. X. 2011, ApJ, 728, 161
Izotov, Y. I., Orlitová, I., Schaerer, D., et al. 2016a, Natur, 529, 178
Izotov, Y. I., Schaerer, D., Thuan, T. X., et al. 2016b, MNRAS, 461, 3683
Izotov, Y. I., Schaerer, D., Worseck, G., et al. 2018a, MNRAS, 474, 4514
Izotov, Y. I., Thuan, T. X., & Lipovetsky, V. A. 1994, ApJ, 435, 647
Izotov, Y. I., Worseck, G., Schaerer, D., et al. 2021, MNRAS, 503, 1734
Izotov, Y. I., Worseck, G., Schaerer, D., et al. 2018b, MNRAS, 478, 4851
Jaskot, A. E., Dowd, T., Oey, M. S., Scarlata, C., & McKinney, J. 2019, ApJ, 885, 96
Jaskot, A. E., & Oey, M. S. 2013, ApJ, 766, 91
Ji, Z., Giavalisco, M., Vanzella, E., et al. 2020, ApJ, 888, 109
Johnson, B. D., Leja, J. L., Conroy, C., & Speagle, J. S. 2019, Prospector: Stellar Population Inference from Spectra and SEDs, Astrophysics Source Code Library, ascl:1905.025
Kennicutt, R. C., & Evans, N. J. 2012, ARA&A, 50, 531
Kroupa, P. 2001, MNRAS, 322, 231
Leclercq, F., Bacon, R., Wisotzki, L., et al. 2017, A&A, 608, A8
Leitet, E., Bergvall, N., Hayes, M., Linné, S., & Zackrisson, E. 2013, A&A, 553, A106
Leitherer, C., Ekström, S., Meynet, G., et al. 2014, ApJS, 212, 14
Leitherer, C., Ferguson, H. C., Heckman, T. M., & Lowenthal, J. D. 1995, ApJL, 454, L19
Leitherer, C., Hernandez, S., Lee, J. C., & Oey, M. S. 2016, ApJ, 823, 64
Leitherer, C., Ortiz Otálvaro, P. A., Bresolin, F., et al. 2010, ApJS, 189, 309
Leitherer, C., Schaerer, D., Goldader, J. D., et al. 1999, ApJS, 123, 3
Leja, J., Johnson, B. D., Conroy, C., van Dokkum, P. G., & Byler, N. 2017, ApJ, 837, 170
Luridiana, V., Morisset, C., & Shaw, R. A. 2015, A&A, 573, A42
Makan, K., Worseck, G., Davies, F. B., et al. 2021, ApJ, 912, 38
Martin, C., Barlow, T., Barnhart, W., et al. 2003, Proc. SPIE, 4854, 336
Mason, C. A., Treu, T., Dijkstra, M., et al. 2018, ApJ, 856, 2
Micheva, G., Iwata, I., & Inoue, A. K. 2017, MNRAS, 465, 302
Mostardi, R. E., Shapley, A. E., Steidel, C. C., et al. 2015, ApJ, 810, 107
Naidu, R. P., Tacchella, S., Mason, C. A., et al. 2020, ApJ, 892, 109
Nakajima, K., & Ouchi, M. 2014, MNRAS, 442, 900
Orlitová, I., Verhamme, A., Henry, A., et al. 2018, A&A, 616, A60
Osterbrock, D., & Ferland, G. 2006, Astrophysics of Gaseous Nebulae and Active Galactic Nuclei (Mill Valley, CA: Univ. Science Books)
Paardekooper, J.-P., Khochfar, S., & Dalla Vecchia, C. 2015, MNRAS, 451, 2544
Pahl, A. J., Shapley, A., Faisst, A. L., et al. 2020, MNRAS, 493, 3194
Paoletti, D., Hazra, D. K., Finelli, F., & Smoot, G. F. 2020, JCAP, 2020, 005
Peña-Guerrero, M. A., & Leitherer, C. 2013, AJ, 146, 158
Pilyugin, L. S., Thuan, T. X., & Vílchez, J. M. 2006, MNRAS, 367, 1139
Planck Collaboration, Aghanim, N., Akrami, Y., et al. 2020, A&A, 641, A6
Rasekh, A., Melinder, J., Östlin, G., et al. 2021, arXiv:2110.01626
Razoumov, A. O., & Sommer-Larsen, J. 2010, ApJ, 710, 1239
Reddy, N. A., Steidel, C. C., Pettini, M., & Bogosavljević, M. 2016, ApJ, 828, 107
Rivera-Thorsen, T. E., Dahle, H., Chisholm, J., et al. 2019, Sci, 366, 738
Robertson, B. E., Ellis, R. S., Furlanetto, S. R., & Dunlop, J. S. 2015, ApJL, 802, L19
Schaerer, D., Izotov, Y. I., Verhamme, A., et al. 2016, A&A, 591, L8
Saldana-Lopez, A., Schaerer, D., Chisholm, J., et al. 2022, A&A, in press (arXiv:2201.11800)
Sharma, M., Theuns, T., Frenk, C., et al. 2017, MNRAS, 468, 2176
Siana, B., Shapley, A. E., Kulas, K. R., et al. 2015, ApJ, 804, 17
Stanway, E. R., & Eldridge, J. J. 2018, MNRAS, 479, 75
Steffen, M., Prakapavičius, D., Caffau, E., et al. 2015, A&A, 583, A57
Steidel, C. C., Bogosavljević, M., Shapley, A. E., et al. 2018, ApJ, 869, 123
Steidel, C. C., Pettini, M., & Adelberger, K. L. 2001, ApJ, 546, 665
Storey, P. J., & Hummer, D. G. 1995, MNRAS, 272, 41
Storey, P. J., & Zeippen, C. J. 2000, MNRAS, 312, 813
Trebitsch, M., Blaizot, J., Rosdahl, J., Devriendt, J., & Slyz, A. 2017, MNRAS, 470, 224
van der Walt, S., Colbert, S. C., & Varoquaux, G. 2011, CSE, 13, 22
Vanzella, E., Guo, Y., Giavalisco, M., et al. 2012, ApJ, 751, 70
Vanzella, E., de Barros, S., Vasei, K., et al. 2016, ApJ, 825, 41
Vanzella, E., Nonino, M., Cupani, G., et al. 2018, MNRAS, 476, L15
Verhamme, A., Orlitová, I., Schaerer, D., & Hayes, M. 2015, A&A, 578, A7
Verhamme, A., Orlitová, I., Schaerer, D., et al. 2017, A&A, 597, A13
Virtanen, P., Gommers, R., & Oliphant, T. 2020, NatMe, 17, 261
Wang, B., Heckman, T. M., Leitherer, C., et al. 2019, ApJ, 885, 57
Wang, B., Heckman, T. M., Amorín, R., et al. 2021, ApJ, 916, 3

Wise, J. H., Demchenko, V. G., Halicek, M. T., et al. 2014, MNRAS, 442, 2560
Wisotzki, L., Bacon, R., Blaizot, J., et al. 2016, A&A, 587, A98
Worseck, G., Prochaska, J. X., Hennawi, J. F., & McQuinn, M. 2016, ApJ, 825, 144
Wyithe, J. S. B., & Loeb, A. 2013, MNRAS, 428, 2741
Yang, H., Malhotra, S., Gronke, M., et al. 2017, ApJ, 844, 171
Yang, J., Wang, F., Fan, X., et al. 2020, ApJ, 904, 26
York, D. G., Adelman, J., Anderson, J. E. J., et al. 2000, AJ, 120, 1579
Zackrisson, E., Inoue, A. K., & Jensen, H. 2013, ApJ, 777, 39
Zackrisson, E., Binggeli, C., Finlator, K., et al. 2017, ApJ, 836, 78